Title

Splicing Factor SRSF1 Deficiency in the Liver Triggers NASH-like Pathology via R-Loop Induced DNA Damage and Cell Death

Authors

Waqar Arif [1,2], Bhoomika Mathur[3], Michael F. Saikali[4], Ullas V. Chembazhi[1], Steven M. Blue[5,6], Brian A. Yee[5,6], Eric L. Van Nostrand[5,6†], Sushant Bangru[1,8], Qinyu Hao[7], Gene W. Yeo[5,6], Kannanganattu V. Prasanth[7,8], Sayeepriyadarshini Anakk[3,8], Carolyn L. Cummins[4], Auinash Kalsotra[1,8,9*]

Affiliations

[1]Department of Biochemistry, University of Illinois Urbana-Champaign, Urbana, IL, USA.
[2]College of Medicine, University of Illinois at Urbana-Champaign, Urbana, IL, USA.
[3]Department of Molecular and Integrative Physiology, University of Illinois Urbana-Champaign, Urbana, IL, USA.
[4]Department of Pharmaceutical Sciences, Leslie Dan Faculty of Pharmacy, University of Toronto, Toronto, Ontario, Canada.
[5]Department of Cellular and Molecular Medicine, University of California at San Diego, La Jolla, CA, USA.
[6]Institute for Genomic Medicine, University of California at San Diego, La Jolla, CA, USA.
[7]Department of Cell and Developmental Biology, University of Illinois Urbana-Champaign, Urbana, IL, USA.
[8]Cancer Center @ Illinois, University of Illinois Urbana-Champaign, Urbana, IL, USA.
[9]Carl R. Woese Institute of Genomic Biology, University of Illinois Urbana-Champaign, Urbana, IL, USA.

***Correspondence to:** Auinash Kalsotra, Ph.D.
506 South Mathews Ave, Medical Sciences Building, Room 462, Urbana, IL 61801
Phone: 217-300-5531; Fax: 217-244-5858; E-mail: kalsotra@illinois.edu

[†]Present address: Department of Biochemistry and Molecular Biology, Baylor College of Medicine, Houston, TX, USA.

Abstract

Regulation of RNA processing contributes profoundly to tissue development and physiology. Here, we report that serine-arginine-rich splicing factor 1 (SRSF1) is essential for hepatocyte function and survival. Although SRSF1 is mainly known for its many roles in mRNA metabolism, it is also crucial for maintaining genome stability. We show that acute liver damage in the setting of targeted SRSF1 deletion in mice is primarily mediated by the excessive formation of deleterious RNA–DNA hybrids (R-loops), which induce DNA damage. Combining hepatocyte-specific transcriptome, proteome, and RNA binding analyses, we demonstrate that widespread genotoxic stress following SRSF1 depletion results in global inhibition of mRNA transcription and protein synthesis, leading to impaired metabolism and trafficking of lipids. Lipid accumulation in SRSF1-deficient hepatocytes is followed by necroptotic cell death, inflammation, and fibrosis, resulting in NASH-like liver pathology. Importantly, SRSF1-depleted human liver cancer cells recapitulate this pathogenesis illustrating a conserved and fundamental role for SRSF1 in preserving genome integrity and tissue homeostasis. Thus, our study uncovers how accumulation of detrimental R-loops impedes hepatocellular gene expression, triggering metabolic derangements and liver failure.

Introduction

The liver is a major workhorse performing hundreds of diverse functions that include detoxifying blood of potentially harmful drugs, producing bile for fat absorption, and processing nutrients to meet metabolic demands during fasting and fed states (*1*, *2*). Therefore, it is not surprising that dysfunction of the liver is associated with poor prognosis and high rates of mortality (*3*, *4*). Besides viral infections, excessive alcohol consumption and nonalcoholic fatty liver disease are the biggest risk factors for hepatic failure. Particularly, the prevalence of nonalcoholic fatty liver disease is rapidly increasing worldwide, posing a significant public health threat (*5–7*). The disease starts with an excess buildup of fat within the liver, but as the condition worsens, the fat deposition (steatosis) is accompanied by severe inflammation (hepatitis) and scarring (fibrosis) that leads to cirrhosis and, finally, hepatocarcinogenesis (*8*). The disease is then referred to as Non-Alcoholic Steatohepatitis (NASH).

Hepatocytes, which are highly differentiated and quiescent cells, are the primary functional units of the liver. While most gene expression studies focus on transcriptional control of hepatocyte function and development, several recent studies have highlighted critical roles for post-transcriptional gene regulatory mechanisms (*9–14*). These mechanisms, which include mRNA capping, splicing, polyadenylation, and editing, are coordinated by a complex interplay between mRNA and RNA binding proteins (RBPs), and in general, control the expression of transcripts by altering their sequence, stability, localization, or translation efficiency (*15–17*). The conserved SR protein family, which includes 12 canonical members, are well-characterized RBPs that regulate multiple aspects of mRNA metabolism. They all share conserved modular structural elements consisting of either one or two N-terminal RNA recognition motifs, which define their RNA sequence binding specificity, and a C-terminal arginine- and serine-rich domain (*18*). Because the genetic deletion of many SR proteins is embryonically lethal, their physiological roles *in vivo* are largely unexplored. However, the latest studies using conditional deletion models are now

highlighting the importance of SR proteins in maintaining liver homeostasis. For example, hepatocyte-specific deletion of *Srsf2* and *Srsf3* in mice resulted in acute liver damage with defects in metabolic functions (*19*, *20*). Likewise, *Srsf10* has also been implicated in liver dysfunction with reduced levels leading to increased hepatic lipogenesis and steatosis (*21*).

Of the SR protein family, SRSF1 (ASF/SF2) was the first to be identified and is considered the archetype member. Though initially characterized as a splicing factor, SRSF1 has since been found to regulate nearly every aspect of mRNA lifecycle, including mRNA transcription, non-sense mediated decay (NMD), mRNA export, and translation (*22–24*). In addition to mRNA metabolism, SRSF1 is also involved in other biological functions such as microRNA processing, maintaining genomic stability, and nucleolar stress (*24*, *25*). The first glimpse of SRSF1's role in tissue physiology began with *in vivo* investigation in mice hearts. Cardiomyocyte-specific deletion of *Srsf1* in mice resulted in missplicing of the Ca^{2+}/calmodulin-dependent kinase IIδ, leading to severe defects in excitation-contraction coupling and heart failure (*26*). Additional studies since then have shown SRSF1 involvement in T-cell differentiation, vascular smooth cell proliferation, and skeletal muscle development (*27–31*). Furthermore, SRSF1 levels are elevated in many different cancers, and it is considered a proto-oncogene (*32–34*). Indeed, orthotopic transplantation of mouse mammary epithelial cells overexpressing SRSF1 is sufficient to promote tumorigenesis (*35*, *36*). While SRSF1 is well-studied in the context of cancer and cardiac physiology, its function in the liver is not well understood.

Here, we generated constitutive and inducible mice models of hepatocyte-specific *Srsf1* deletion to define its *in vivo* function in liver physiology. We found that SRSF1 inactivation is detrimental for cell viability and triggers NASH-like pathology. Mechanistically, we show that SRSF1-deficient hepatocytes accumulate deleterious RNA-DNA hybrids (R-loops) and develop extensive DNA damage. The overwhelming damage results in transcriptional inhibition, diminished protein synthesis, metabolic insufficiency, and cell death, inducing a compensatory

regenerative response that gradually repopulates the liver with SRSF1-expressing hepatocytes. Importantly, transient knockdown of SRSF1 in human liver cancer cells recapitulates the molecular pathogenesis identified in the animal models. Thus, our findings uncover new interconnections between genome stability, hepatocellular gene expression, and intermediary metabolism.

Results

Hepatic knockout of SRSF1 triggers immediate repopulation with SRSF1-expressing hepatocytes

To investigate the role of SRSF1 in liver physiology, we disrupted its expression in hepatocytes by crossing *Srsf1*$^{flox/flux}$ with *AlbCre* transgenic mice. Although hepatocyte-specific SRSF1 knockout (SRSF1 HKO) mice were born at the expected Mendelian ratio and survived to adulthood, their livers displayed gross morphological defects during the early postnatal stages. At postnatal day (PN) 10, SRSF1 HKO livers were highly pale and yellow in color, signifying severe fatty infiltration of the tissue, referred to as steatosis **(Fig. 1A)**. SRSF1 HKO mice also appeared to have stunted growth which is evident from their decreased weight trend in comparison to littermate controls (fig. S1A, B). Histological analysis of the liver tissue sections at early postnatal timepoints showed that, up to PN6, both SRSF1 HKO and control mice had similar lipid content. However, beyond this time point, lipid accumulation persisted in SRSF1 HKO livers, whereas in control mice the lipid content had diminished **(Fig. 1B)**. Furthermore, hepatocyte damage and death were evident starting at PN6 and continued through later timepoints (fig. S1C). Surprisingly, despite the drastic liver phenotype, SRSF1 levels in the knockout model at PN10 displayed only a two-fold reduction (fig. S1B). This finding was unexpected because previous reports utilizing a Cre-dependent reporter have shown uniform *AlbCre* transgene activity across all hepatocytes by PN3 (*37*, *38*). Hence, a greater reduction of SRSF1 was anticipated in the knockout model.

To determine the basis of this discrepancy, we performed immunofluorescent co-staining for SRSF1 and the hepatocyte marker HNF4α on liver sections at early postnatal timepoints **(Fig. 1B)**. The greatest decrease in SRSF1 expression within hepatocytes was observed at PN6, which coincided with the onset of damage and steatosis detected histologically. After this time point, SRSF1-deficient hepatocytes were slowly replaced by an expanding population of SRSF1-positive hepatocytes **(Fig. 1C)**. We hypothesized that the parenchymal repopulation with SRSF1 expressing

hepatocytes resulted either from expansion of wildtype hepatocytes that have escaped Cre-mediated SRSF1 knockout and/or continuous transdifferentiation of biliary epithelial cells (BEC) into hepatocytes. Irrespective of the mechanism, an increase in hepatic proliferation would be required to sustain the steady repopulation. As predicted, increased immunostaining of hepatocyte nuclei with Ki67, a marker of cell proliferation, was observed in SRSF1 HKO mice at PN10 (fig. S1C-D). While increased proliferation at early stages is expected, later stage phenotypes are anticipated to differ depending on the mechanism of hepatocyte repopulation. For instance, if hepatocytes were escaping Cre-mediated knockout of *SRSF1*, the livers would repopulate with SRSF1 expressing hepatocytes, leading to normalization of liver function over time. Conversely, if transdifferentiation of BECs to hepatocytes was the primary mechanism, chronic injury and eventual liver failure would be likely as transdifferentiated hepatocytes would cycle through continuous cell death.

To determine the primary mechanism of hepatocyte repopulation in SRSF1 HKO livers, we performed immunofluorescence and RT-qPCR analysis at later time points. In agreement with the first mechanism, quantification of SRSF1-expressing hepatocytes at 1- and 3-months revealed a steady repopulation of the liver parenchyma **(Fig. 2A)**. Specifically, at 1 month, the SRSF1 HKO livers were nearly 60% repopulated with SRSF1-expressing hepatocytes, and by 3 months, the repopulation was essentially complete. This finding correlated well with the gradual reversal of pathological changes detected in juvenile SRSF1 HKO mice (fig. S2A-D). For instance, SRSF1 HKO had stunted growth with lower total body and adipose weights at 1 and 3 months. However, by 6 months, these differences normalized to littermate controls as liver function was restored.

The phenomenon of liver repopulation with wildtype hepatocytes in a hepatocyte-specific conditional knockout mouse model has been previously reported. *Sekine et al.* found that hepatocyte-specific deletion of *Dicer1* results in overwhelming cell death followed by regeneration and progressive repopulation with DICER1-expressing hepatocytes (*39*). Further, they demonstrated that the repopulating hepatocytes had escaped *Dicer1* knockout by silencing the

expression of the *Cre* transgene. Therefore, to assess if *Cre* silencing was occurring in SRSF1 HKO, the abundance of *Cre* mRNA was measured using qRT-PCR at PN4, 1-month, and 3-month time points **(Fig. 2B)**. Notably, compared to controls, the SRSF1 HKO livers showed a striking downregulation of *Cre* expression over time, thus allowing *SRSF1* to remain intact. These data provide strong evidence for progressive repopulation of SRSF1 HKO livers with hepatocytes that have escaped Cre-mediated recombination.

SRSF1 HKO mice exhibit acute and reversible NASH-like liver injury

Although SRSF1 HKO livers began to overcome Cre-mediated knockout early in postnatal development, these mice still displayed severe liver dysfunctions at adult stages. Histological analysis of SRSF1 HKO livers at 1-, 3- and 6-month time points presented pathology comparable to the human disease known as Nonalcoholic steatohepatitis, or NASH **(Fig. 3A-C)**. Key hallmarks of NASH include the progressive development of steatosis, ballooning degeneration, necroinflammation and perisinusoidal fibrosis (*40*, *41*). At 1-month, widespread injury was detected with necrotic and ballooning hepatocytes accompanied with infiltrating inflammatory cells **(Fig. 3A)**. However, the damage and inflammation were drastically reduced at later time points. Similarly, significant lipid accumulation was observed at 1 and 3 months, but by 6 months, the steatosis was strikingly diminished **(Fig. 3B)**. A defining feature of NASH is scar tissue formation, or fibrosis, as the liver attempts to repair the injured tissue (*40*). As anticipated, fibrosis was detected in SRSF1 HKO mice with peak fibrosis seen at three-months and slight bridging fibrosis at six-months **(Fig. 3C)**. But, unlike NASH, where damage worsens with time, SRSF1 HKO liver injury subsided with age and the mice recovered as *SRSF1*-expressing hepatocytes repopulated the liver.

Consistent with the histological findings, liver function and metabolic tests in SRSF1 HKO indicated chronic injury with eventual normalization (Table S1 and fig. S2E). For instance, serum ALT and AST levels were drastically elevated at 1 month, signifying liver damage, but the levels gradually decreased with age and by 6 months were indistinguishable from controls. On the other

hand, serum triglycerides and cholesterol levels showed the opposite trend with decreased levels at early ages, which increased to baseline by 6 months. This is expected since the liver is involved with lipid trafficking and cholesterol synthesis. Despite abnormal liver function tests, glucose metabolism remained intact in SRSF1 HKO indicated by their normal fasting glucose levels and glucose tolerance tests (Table S1 and fig. S2E). Altogether, these findings demonstrate that liver damage in SRSF1 HKO mice occurs in two phases consisting of (1) acute injury which begins immediately after birth and (2) chronic injury that lasts about three months, at which point the liver is completely repopulated with *SRSF1*-expressing hepatocytes.

Hepatic ablation of SRSF1 induce inflammatory and fibrotic gene signatures

To study transcriptome changes in SRSF1 HKO during both early and late phases of injury, we performed RNA sequencing (RNA-seq) on isolated hepatocytes from PN10 (early) and 1 month (late) old mice. Differential gene expression analysis using DESeq2 showed drastic changes in mRNA abundances ($|\log_2\text{FoldChange}| \geq 1$, FDR < 0.10) at both early and late timepoints with approximately 8.6% and 10.0% of expressed hepatic genes affected, corresponding to 1,825 and 1,902 transcripts, respectively **(Fig. 4A)**. Furthermore, a larger fraction of differentially expressed genes (DEGs) increased in expression, with ~63% at the early and ~79% at the late phases respectively. DEGs shared between the early and late time points encompassed 544 genes corresponding to about one-third of either gene sets. Although the expression of the overlapping gene set had a strong linear correlation ($R^2_{pearson} = 0.647$), the degree of fold change tended to be greater during the late phase **(Fig. 4B)**. Hence, genes that were upregulated early were further potentiated during the late phase.

As substantial alterations to the transcriptome were triggered in response to SRSF1 deletion, we hypothesized these changes are induced to mitigate the hepatic insufficiency and injury resulting from the loss of SRSF1 activity. To identify biological processes associated with the transcriptome changes, gene ontology enrichment analysis was performed on DEGs in SRSF1 HKO **(Fig. 4C)**.

Genes upregulated during the acute phase in SRSF1 HKO were highly enriched for inflammatory processes such as chemokine signaling and leukocyte migration. This is expected as widespread cell death frequently triggers inflammation to promote cellular recruitment for tissue repair. Indeed, infiltration of inflammatory cells into the tissue parenchyma was seen in SRSF1 HKO at the late time point. However, the inflammation resolved as the liver repopulated with SRSF1-expressing hepatocytes, resulting in decreased necrosis and wound healing. This response pattern was further corroborated by the expression profiles of various inflammatory and fibrosis markers **(Fig. 4D)**. Of note, genes upregulated at the later time point were primarily involved in cell division and mitotic processes, which points to the compensatory regenerative response occurring in the SRSF1 HKO livers **(Fig. 4C)**. Conversely, transcripts downregulated at either time point in SRSF1 HKO were associated with key metabolic pathways. During the early phase, pathways involved in sterol transport and fatty acid oxidation was downregulated, whereas the late phase encompassed downregulation of sulfur amino acid, ornithine, and urea metabolism. In general, this suggests that SRSF1 HKO livers exhibit reduced metabolic capacity **(Fig. 4C)**. Collectively, our data show that hepatic loss of SRSF1 triggers a robust expression of transcripts to facilitate inflammation, which then gradually transition to proliferative and wound healing processes as the liver regenerates.

Considering that SRSF1 is a canonical splicing factor, loss of its activity is anticipated to result in extensive splicing defects. Using rMATS, a computational tool for quantifying differential splicing from RNA-seq, we identified 852 and 765 significantly changing splicing events (ΔPSI > 15%; FDR < 0.10) at the early and late phases, respectively (fig. S3A-B). The transcripts with differentially spliced exons (DSE) were enriched in a wide variety of functions ranging from metabolic processes to chromosomal organization (fig. 4C). However, due to the acute injury and regenerative response in this model, interpretation of these findings is complicated and likely reflects secondary changes to liver injury and damage. Therefore, to identify the molecular events

leading to damage upon SRSF1 ablation, a model was required which would allow capturing SRSF1-deficient hepatocytes before the onset of the injury.

Acute hepatic knockout of SRSF1 in adult mice recapitulates SRSF1 HKO pathology

We developed an additional model which allows for acute knockout of SRSF1 in hepatocytes of adult mice (acSRSF1 HKO). This was achieved using adeno-associated viral vectors expressing the Cre recombinase driven by the hepatocyte-specific thyroxine binding globulin (TBG) promoter **(Fig. 5A)**. A benefit of this model is that it allows the study of primary molecular changes resulting from SRSF1 depletion by permitting the isolation of SRSF1-deficient hepatocytes before the development of pathology. Robust depletion of SRSF1 protein was achieved in the livers of adult mice after 2 weeks of AAV8-TBG-iCre viral vector transduction **(Fig. 5B)**. Prior to performing in-depth molecular studies on acSRSF1 HKO mice, we verified if this model develops liver pathology like SRSF1 HKO mice. Histological staining revealed mild microsteatosis at the 2-week time point with lipid droplets distributed near the central vein hepatocytes. Importantly, there was no evidence of damage or fibrosis at this time point (fig. S4A). By 4 weeks, acSRSF1 HKO livers displayed severe lipid accumulation with macrosteatosis throughout the tissue parenchyma. In addition, signs of cell death with ballooning degenerating hepatocytes were noted. To verify if the dying hepatocytes were initiating apoptosis, we performed TUNEL staining on liver tissue sections (fig. S4B). The staining showed no positive cells, suggesting that SRSF1-deficient hepatocytes were likely undergoing necrotic cell death. Despite the severe steatosis and damage by 4 weeks, acSRSF1 HKO mice did not exhibit any overt liver inflammation or fibrosis. These findings demonstrate that acSRSF1 HKO mice develop severe steatosis followed by necrosis, recapitulating the pathological progression seen in SRSF1 HKO mice.

A limitation of the SRSF1 HKO model was the early regenerative response and repopulation with SRSF1-expressing hepatocytes. While western blot analysis of acSRSF1 HKO livers showed efficient knockout of SRSF1 at 2 weeks, like the SRSF1 HKO model, re-expression of SRSF1 was

noted by 4 weeks **(Fig. 5B)**. To validate that this re-expression was due to the repopulation of the liver with SRSF1-expressing hepatocytes, immunofluorescence co-staining was performed on tissue sections **(Fig. 5C)**. Indeed, the staining showed reappearance of SRSF1-positive hepatocytes. Nonetheless, despite this repopulation, the acSRSF1 HKO model provided the opportunity to study SRSF1-deficient hepatocytes before the onset of damage.

AcSRSF1 HKO mice develop acute hepatic failure

Next, we sought to understand the physiological changes occurring in the acSRSF1 HKO mice. We began by assessing changes in total body, liver, and adipose tissue mass following viral transduction **(Fig. 5D)**. We found that acSRSF1 HKO mice maintained their body weight for up to 2 weeks, which then fell dramatically by 4 weeks. On average, acSRSF1 HKO mice lost ~15% of their starting total body weight, whereas control mice gained ~5% after 4 weeks. Regarding the liver and adipose tissue, we found that their masses trended reciprocally to each other **(Fig. 5E-F)**. In agreement with the observed steatosis and hepatocyte dysfunction, liver mass steadily increased with time while adipose stores diminished. Given the notable steatosis, we wondered if the accumulating lipids primarily consisted of triglycerides or cholesterol **(Fig. 6A)**. Therefore, total hepatic lipids were extracted from whole liver tissue, followed by quantification using colorimetric assays. Our measurements showed progressively elevated levels of hepatic triglycerides at 2- and 4-weeks in acSRSF1 HKO mice and simultaneous reductions in cholesterol levels **(Fig. 6B)**. To further evaluate the hepatic dysfunction in acSRSF1 HKO mice, biochemical profiling of the serum was performed **(Fig. 6C)**. Measurement of serum ALT and AST activity, markers of liver injury, showed no significant difference at the 2-week time point between acSRSF1 HKO and control mice. However, by 4 weeks, their levels were strikingly elevated, signifying severe liver damage. This was also evident by the golden yellow appearance of the serum due to elevated bilirubin levels resulting from decreased clearance by the liver (fig. S4C).

Importantly, acSRSF1 HKO mice did not exhibit significant differences at 2 weeks for any of the measured serum parameters **(Fig. 6C)**. These findings further support that this time point precedes any detectable damage and secondary effects. On the other hand, serum profiling of 4-week acSRSF1 HKO mice serum showed severe metabolic derangements. For instance, fasting glucose levels in acSRSF1 HKO were lower than normal, with an average concentration of 65 mg/dL at 4 weeks, signifying impaired gluconeogenesis. In a fasted state, the liver generates ketone bodies as an alternative energy source reflected by their elevated serum levels. However, we noticed that ketone bodies in acSRSF1 HKO were strikingly diminished at 4 weeks despite being in a fasted state. In agreement with the decreased cholesterol in hepatic tissue, acSRSF1 HKO also showed declining serum cholesterol levels. This is expected with widespread liver damage since cholesterol is predominantly synthesized by hepatocytes. Likewise, fractionated serum profiles of 4-week acSRSF1 HKO mice showed marked depletion of lipoprotein particles that are synthesized and secreted by hepatocytes for systemic transport of lipids (fig. S4D). These findings explain the decreased serum phospholipid concentrations since they are mainly circulated within lipoprotein particles **(Fig. 6C)**. Finally, no significant differences were observed in serum concentrations of triglycerides and non-esterified fatty acids. Altogether, these results suggest that hepatic loss of SRSF1 leads to severe metabolic insufficiency and eventual hepatic failure.

SRSF1 deficiency leads to global defects in the transcriptome

Given that SRSF1 regulates multiple aspects of mRNA metabolism, we reasoned that widespread defects to the transcriptome drive the cellular demise upon SRSF1 knockout. To effectively identify early transcriptome defects, we performed an RNA-seq study on hepatocytes isolated from acSRSF1 HKO at the 2-week time point. Unexpectedly, we found 3,717 mRNA transcripts changing in abundance and 2,996 transcripts changing in splicing following acute ablation of SRSF1 in adult hepatocytes (fig. S5A-C). Compared to the SRSF1 HKO model, these changes correspond to a 104% and 252% increase in the number of mRNA abundance and splicing

events, respectively. While we understand that comparisons between these two datasets is not ideal, nonetheless, we were surprised by the number of transcriptome alterations in the acSRSF1 HKO model. Of the mRNAs changing in abundance, ~68% were upregulated, corresponding to 2,525 transcripts. In terms of alternatively spliced events, we detected changes in 2040 skipped exons, 252 retained introns, 354 mutually exclusive exons, 156 alternative 3' splice sites, and 194 alternative 5' splice sites. As expected, over two-thirds of skipped exons exhibited decreased inclusion, since SRSF1 tends to promote exon inclusion. Overall, these findings provide strong evidence that the transcriptome defects caused by SRSF1 knockout precede the onset of damage and inflammation.

To further explore if the observed splicing defects in the acSRSF1 HKO model are directly regulated by SRSF1, we performed eCLIP-seq to profile SRSF1-binding distributions on transcripts in hepatocytes. Two independent eCLIP libraries were prepared and sequenced with excellent reproducibility between the replicates indicated by a high correlation in gene read counts ($R_{spearman}$ = 0.941, p-value < 1 x 10^{-15}). Using the CLIPper peak calling tool, we detected a total of 5,272 SRSF1 binding peaks between the two replicates (*42*). We found nearly two-thirds (~64%) of the binding peaks mapped to either exon or exon-intron boundary sequences (fig. S5D). In addition, gene ontology analysis of SRSF1-bound transcripts showed enrichment for RNA binding proteins and metabolic processes such as lipoprotein particle and sterol transport (fig. S5E). Importantly, SRSF1 binding peaks in mouse hepatocytes were enriched with the GAAGAA consensus sequence motif established in previously published SRSF1 binding studies (fig. S5F). Next, we identified SRSF1 binding peaks that were in proximity to DSEs found in acSRSF1 HKO mice. If the mis-spliced exons in acSRSF1 HKO were dependent on SRSF1's splicing activity, there would be an enrichment of SRSF1 binding peaks in and around DSEs. To our surprise, less than 6% of the binding peaks localized within DSEs (fig. S5G). Conversely, examining the spatial binding distribution of SRSF1 on the 2,040 differentially skipped exons in acSRSF1 HKO revealed a

striking de-enrichment in binding in comparison to a control set of constitutive exons (fig. S5H). Collectively, these findings suggest that the majority of transcriptome defects arising after acute SRSF1 deletion are independent of its splicing activity and likely result from defects in mRNA transcription, export, stability, and/or translation.

The Unfolded Protein Response is not activated upon SRSF1 knockout

Given the presence of aberrant transcripts in acSRSF1 HKO and SRSF1's role in promoting NMD, a possible mechanism of hepatocyte failure is an accumulation of unfolded proteins leading to ER stress and activation of the unfolded protein response, or UPR (*43–45*). To explore this hypothesis, we began by examining expression changes in acSRSF1 HKO of genes known to be upregulated in the setting of UPR activation (fig. S6A). However, as is evident from the heatmap, there was a downregulation of UPR responsive genes, suggesting a lack of UPR activation. We also assessed UPR activation by measuring protein levels of the transcription factor CHOP and by quantifying the splicing of *Xbp1* mRNA into its short isoform (*46*, *47*). We found that both CHOP protein levels and *Xbp1* mRNA splicing were unchanged in acSRSF1 HKO hepatocytes (fig. S6B-C), further confirming that ER stress and UPR activation are not the direct triggers of hepatocyte death in acSRSF1 HKO livers.

Loss of SRSF1 leads to R-loop accumulation and widespread DNA damage

To gain further insight into the biological processes affected by the transcriptome perturbations in acSRSF1 HKO hepatocytes, we performed an integrated gene ontology analysis using genes changing in expression and splicing. We constructed a GO network where each node corresponds to an enriched biological process. The size and color represent the number of genes within each node and the overall direction of differential expression, respectively (**Fig. 7A**). Furthermore, nodes with a blue outline signify ≥10% of the associated genes exhibited differential splicing. Similar to the chronic model, acSRSF1 HKO displayed a strong enrichment for immune processes indicating that loss of SRSF1 in hepatocytes triggers the necessary signals for recruitment

and activation of inflammatory cells before the onset of damage. We also noticed simultaneous induction of genes associated with regeneration, angiogenesis, and proliferation-related functions. With cell death and declining hepatic function(s) in acSRSF1 HKO, this is likely a compensatory response to ensure timely repopulation of the liver tissue with healthy hepatocytes.

The GO network also revealed strong upregulation and impaired splicing of genes associated with apoptosis and DNA repair pathways (**Fig. 7A**). Accordingly, we hypothesized that overwhelming DNA damage might be the primary cause of hepatocyte death in SRSF1-deficient livers. A previous study identified SRSF1 as a crucial factor in maintaining genome stability wherein SRSF1 depletion in DT40 cells caused widespread and unresolvable DNA damage due to the accumulation of genotoxic RNA-DNA hybrid structures known as R-loops (*25*). While these structures are considered as byproducts of transcription, their occurrence in most cells are rare and readily resolved by dedicated enzymes (*48*). Growing evidence suggests that co-transcriptional splicing factors, such as SRSF1, facilitate the release of nascent RNA from the template DNA to counteract R-loop formation.

To determine if DNA damage is present in acSRSF1 HKO hepatocytes, we performed immunofluorescent staining on liver tissue sections from Control and acSRSF1 HKO mice for γH2A.X, a well-known marker of DNA damage (*49*). In agreement with our hypothesis, we observed robust staining of γH2A.X foci only in the hepatocyte nuclei of acSRSF1 HKO mice (**Fig. 7B**). Furthermore, γH2A.X-positive nuclei were readily detected in SRSF1 HKOs at the 10-day and 1-month time points as well. Next, we set out to confirm if SRSF1-deficient hepatocytes display elevated levels of R-loops. We performed a dot blot assay using the S9.6 antibody, which recognizes RNA-DNA hybrids, on DNA isolated from Control and acSRSF1 HKO hepatocytes (**Fig. 7C**). SRSF1-deficient hepatocytes showed strikingly elevated levels of RNA-DNA hybrids, most likely due to the increased formation of R-loops.

Accumulation of R-loops can severely impair transcriptional dynamics. These highly stable hybrid structures can interfere with transcription by directly blocking the activity of RNA polymerase. With R-loop-induced DNA damage *in vivo*, transcription is further impacted as DNA damage triggers phosphorylation and ubiquitination of RNA polymerase II, resulting in global transcriptional repression. To assess the global transcriptional activity of SRSF1-deficient hepatocytes, we performed a polydT dot blot assay on equally loaded total RNA and evaluated differences in steady-state levels of polyA mRNA between Controls and SRSF1-deficient hepatocytes (**Fig. 7D**). Since total RNA is primarily composed of rRNA (~80%), which has a longer half-life than mRNA (days versus minutes, respectively), we expected this assay would allow for a detectable decrease in polyA signal in the setting of global transcriptional repression. Indeed, a significant reduction in polyA-to-total RNA signal ratio was observed in SRSF1-deficient hepatocytes relative to Control hepatocytes. Specifically, we detected a fold change in the signal ratio of 0.64 and 0.74 in 2-week acSRSF1 HKO and 10-day SRSF1 HKO mice, respectively. Collectively, these data provide compelling evidence that SRSF1 deficiency results in excessive accumulation of R-loops, resulting in subsequent DNA damage and global transcription repression.

SRSF1-deficient hepatocytes display diminished global translation

Given the decreased level of total mRNA in SRSF1-deficient hepatocytes, we expected the hepatic proteome to be markedly affected. To study changes in the hepatic proteome resulting from SRSF1 deficiency, we performed quantitative high-throughput mass spectrometry analysis on hepatocytes from control and acSRSF1 HKO mice. We detected a total of 3,603 distinct proteins, with 613 and 159 of the detected proteins significantly decreasing and increasing in relative abundance ($Log_2|IBAQ\ ratio| > 1$, adjusted p-value < 0.10), respectively (fig. S7A). We also noted that aside from SRSF4, which was mildly elevated, all other SR protein levels remained stable and did not undergo a compensatory increase in abundance following SRSF1 deletion (fig. S7B). Overall, nearly 80% of differentially abundant proteins (DAPs) in acSRSF1 HKO hepatocytes

exhibited reduced levels. Furthermore, it is known that SRSF1 can associate with polyribosomes and promote the translation of target mRNAs in an mTOR-dependent manner (*50*, *51*). However, we found that only ~16% of DAPs in acSRSF1 HKO demonstrated binding of SRSF1 on the associated transcript with no enrichment for downregulated proteins as would be expected (fig S8C-D). Moreover, the intersection of DAPs with mRNAs changing in abundance and splicing showed a modest overlap of ~18% and ~14%, respectively (fig. S7E-F).

Next, we utilized gene ontology analysis to understand the various processes affected by the altered proteome of SRSF1-deficient hepatocytes (fig. S7G). Surprisingly, our results showed that proteins with decreased abundances strongly enriched for factors involved in translation. Specifically, a striking depletion was observed for ribosomal proteins, tRNA synthetases, and translation initiation factors with no significant change in expression of the associated mRNA (**Fig. 8A**). Because acSRSF1 HKO displayed widespread depletion of essential elements necessary for mRNA translation, we reasoned this would result in the failed assembly of the ribosomal complex. This was further validated by hepatocyte-specific polysome profiling, which showed an absence of polysomal peaks in acSRSF1 HKO, indicative of impaired ribosomal elongation (fig. S7H). To further quantify overall protein synthesis rates *in vivo*, we pulse-labeled control and acSRSF1 HKO mice at the 2-week time point with puromycin followed by immunoblotting with an anti-puromycin antibody (i.e., SUnSET assays) (*52*). We detected a robust decrease in puromycin labeled peptides in acSRSF1 HKO, signifying lower protein synthesis rates relative to control hepatocytes (**Fig. 8B**). Spleen was used as a control tissue which showed no difference in puromycin incorporation. The reduction in global protein synthesis could be attributed to a generalized stress response, which is facilitated by phosphorylation of the α subunit of the eukaryotic translation initiation factor 2 (eIF2α) at serine S51 (*53*). However, acSRSF1 HKO mice did not exhibit an increase in eIF2α phosphorylation (**Fig. 8C**). Instead, a decrease in phosphorylated eIF2α was noted in 4-week

acSRSF1 HKO and 10-day SRSF1 HKO hepatocytes, which likely reflects regeneration-associated surge in protein synthesis (*54*, *55*).

Because SRSF1 ablation resulted in severe depletion of mRNAs and proteins, we anticipated that SRSF1-deficient hepatocytes would likely become inactive and be eventually eliminated. Given the absence of apoptosis indicated by the negative TUNEL staining, we posited that SRSF1-deficient hepatocytes may be undergoing a necrotic death. This notion was supported by the histological features of swollen hypochromic cells with intact nuclei in SRSF1 HKO livers. To further confirm the mode of cell death in acSRSF1 HKO, we measured the levels of BAX and RIPK1 proteins, which are markers of apoptosis and necrosis, respectively (**Fig. 8C**) (*56*, *57*). Interestingly, both BAX and RIPK1 were elevated in 4-week acSRSF1 HKO and 10-day SRSF1 HKO hepatocytes. These results indicate that SRSF1-deficient hepatocytes undergo necroptosis—a form of immunogenic programmed cell death—resulting in the release of damage-associated molecular patterns (DAMPs), which signals the recruitment of inflammatory cells and subsequent clearance of cellular debris (*58*). Indeed, the features of inflammation were readily detected both histologically and in the transcriptomic signatures of SRSF1 HKO livers.

Knockdown of SRSF1 in HepG2 reproduce acSRSF1 HKO pathology

We next tested if SRSF1 HKO pathology could be reproduced in the context of human cells. We examined publicly available transcriptome datasets from the ENCODE project of shRNA-mediated knockdowns of SR proteins in HepG2 cells, a human liver cancer cell line (*59*). The differential gene expression and splicing analysis for SRSF1, SRSF3, SRSF5, SRSF7, and SRSF9 depleted cells showed that among all SR proteins, knockdown of SRSF1 had the greatest impact on the transcriptome (Table S2). Gene ontology analysis revealed that downregulated genes in SRSF1 depleted cells were strongly enriched for factors involved in translation and the ribosome complex (fig. S8A-B). This is consistent with our findings of reduced ribosomal proteins and diminished global translation in acSRSF1 HKO hepatocytes.

We also noted that SRSF1 knockdown triggers the induction of many known p53-responsive genes (fig. S8C). In a healthy cell, p53 is maintained at low levels and remains inactive in a complex with MDM2 (*60*). However, upon DNA damage or other stresses, various pathways activate p53 by phosphorylation of its N-terminal domain. This phosphorylation facilitates disassociation of p53 from MDM2, resulting in increased stability and activation of its transcriptional activity, thus, promoting the expression of DNA damage response genes (*61*). Activation of p53 in the setting of SRSF1 depletion is consistent with the widespread DNA damage observed in SRSF1 HKO hepatocytes. As anticipated, both total and phosphorylated p53 levels in 10-day SRSF1 HKO were elevated relative to control hepatocytes (fig. S8D).

Next, we performed siRNA-mediated depletion of SRSF1 in HepG2 cells and found robust activation of p53 within 36 hours of SRSF1 knockdown (fig. S8E). Importantly, similar to SRSF1 HKO models, transient depletion of SRSF1 in HepG2 cells was sufficient to cause R-loop accumulation (fig. S8F), DNA damage, diminished protein synthesis, and eventual cell death (**Fig. 9**). Finally, to test if p53 activation mediates the arrest in protein synthesis in SRSF1 depleted cells, we performed SRSF1 and p53 double knockdowns (fig. S8E). However, reducing p53 in SRSF1 depleted cells did not rescue the defects in protein synthesis or cell death, indicating these phenotypes are p53-independent (**Fig. 9** and fig. S8F). Taken together, these results illustrate that the accumulation of detrimental R loops and subsequent DNA damage responses observed in the SRSF1 HKO mice models are recapitulated in SRSF1-depleted human cells.

Discussion

Since its initial discovery as a splicing factor, SRSF1 has been recognized for its myriad roles in mRNA metabolism, including stability, export, NMD, and translation (*24*, *62*). While SRSF1 is well-characterized biochemically, exactly how its activities impact *in vivo* tissue function(s) is still not fully appreciated. In this study, we define a crucial role for SRSF1 in maintaining genome integrity and we demonstrate how accumulation of R-loops in its absence affects hepatocellular gene expression, triggers severe metabolic dysfunctions, and leads to NASH-like liver pathology. Although we initially set out to understand the role of SRSF1 in maintaining liver physiology, we discovered its broader core function in maintaining cell viability.

Caveats of liver-specific transgenic mice

We began our investigations by studying the effects of SRSF1 ablation on hepatocyte function. Because the whole-body knockout of SRSF1 is embryonically lethal, we generated a Cre-mediated hepatocyte-specific knockout referred to as SRSF1 HKO (*26*). We were surprised to find that SRSF1 HKO mice survived and could maintain viable, functional livers, despite early insufficiencies and damage. However, on further examination, we determined that SRSF1-deficient hepatocytes were undergoing rapid cell death, triggering a compensatory regenerative response. Even more astonishing was that SRSF1 HKO mice livers ultimately evaded the deletion and repopulated their parenchyma with SRSF1-expressing hepatocytes. This repopulation reversed the liver damage, inflammation, and the initial growth delays seen in SRSF1 HKO mice over time.

We identified this resistance to knockout in SRSF1 HKO was due to the suppression of Cre expression (*39*). As for the mechanistic underpinnings of this phenomenon, work by Duncan et al. (2012) provides the most plausible explanation (*63*). A unique feature of liver tissue is that it comprises polyploid or aneuploid hepatocytes, thus, creating increased genetic diversity (*64*, *65*). Duncan et al. elegantly showed that certain conditions of chronic liver injury result in the selection of a differentially resistant aneuploid karyotype leading to adaptation (*63*). With SRSF1 HKO mice,

knockout-resistant aneuploid hepatocytes—that lack the Cre transgene—are likely repopulating the liver. Such an effect is possible in the liver, which has high regenerative capacity and a number of aneuploid cells. On the contrary, ablation of SRSF1 in cardiomyocytes, which have low regenerative potential, resulted in heart failure and death (*26*). Given that the whole-body deletion of *Srsf3* is embryonically lethal, it is highly likely that SRSF3 HKO mice would also exhibit the adaptive mechanisms seen in SRSF1 HKO. In fact, the knockdown of SRSF3 in a human HCC cell line robustly downregulates SRSF1 protein levels due to its aberrant splicing (*66*). Thus, our work illustrates a potential limitation to consider when using liver-specific transgenic animal models.

Mechanism of demise in SRSF1 depleted hepatocytes

We performed a series of experiments to understand the cascade of molecular events leading to hepatocyte death in SRSF1 HKO. Elucidating the mechanism was complicated by the fact that SRSF1 regulates multiple aspects of gene expression. To help dissect the pathogenic process, we developed an acute hepatocyte-specific SRSF1 knockout mouse model, which allowed for a precise temporal control of SRSF1 deletion. As expected, acSRSF1 HKO mice displayed robust hepatocyte cell death with subsequent development of hepatic failure. Importantly, this model permitted us to probe primary changes in SRSF1-deficient hepatocytes before the onset of damage. Using this model, we discovered that SRSF1 depletion caused widespread DNA damage (**Fig. 10**). An often overlooked attribute of SRSF1 is its essential function in maintaining genomic stability. It protects the genome by preventing the formation and accumulation of deleterious R-loops that naturally occur during transcription. In fact, this activity was discovered when depletion of SRSF1 using a tet-repression system in DT40 chicken B cells resulted in extensive cell death followed by an expansion of SRSF1-expressing tet-resistant colonies (*25*). The DT40 cell culture model strongly parallels our findings in SRSF1 HKO mice. Particularly, we found that SRSF1-deficient hepatocytes exhibit reduced transcriptional activity likely due to the combined inhibitory effects of R-loop accumulation and DNA damage response. This ultimately results in diminished protein

synthesis, causing depletion of essential enzymes and hepatic proteins, which impairs metabolism and transport of lipids. We further demonstrated that lipid-laden, metabolically challenged, SRSF1-deficient hepatocytes succumb to necroptotic cell death, triggering inflammation, and fibrosis, thereby provoking a NASH-like liver pathology (**Fig. 10**).

In conclusion, our work underscores a fundamental role for SRSF1 in maintaining genome integrity and cell viability. While our study investigates the effects of SRSF1 depletion in hepatocytes, our findings are broadly applicable to any eukaryotic system. Several groups have recently examined the role of SRSF1 in T cell development, vascular smooth muscle proliferation, and skeletal muscle development utilizing cell-type-specific knockout mice models (*27*, *29–31*). Although the observed outcomes of SRSF1 ablation in these studies were attributed to its alternative splicing activity, our findings suggest these effects are much more complex and potentially secondary to genome instability. For instance, reduced mRNA translation in SRSF1-deficient cells would inhibit NMD and deplete spliceosomal factors that can indirectly lead to missplicing and/or accumulation of aberrantly spliced transcripts. Moreover, there is growing evidence that RNA processing factors serve key roles in protecting the genome from the deleterious effects of transcription (*67*). Initial studies in yeast revealed that disruption of mRNA export factors results in R-loop mediated DNA damage (*68*). This effect has since been shown to result from the disruption of multiple factors involved at various stages of RNA biogenesis (*69*, *70*). Recently, it was reported that knockdown of Slu7, another splicing regulator, in cultured cells and mice livers causes R-loop accumulation and DNA damage (*66*). Intriguingly, depletion of Slu7 evoked missplicing of SRSF1 transcript and subsequent downregulation of SRSF1 protein. Thus, our work supports the emerging notion of RNA processing factors moonlighting as guardians of the genome.

Materials and Methods

Generation of SRSF1 HKO and acSRSF1 HKO. *Srsf1*$^{flox/flox}$ mice were crossed with transgenic *AlbCre* mice (C57BL6/J background; The Jackson Laboratory, Bar Harbor, Maine, USA), in which expression of Cre recombinase is driven by the hepatocyte-specific albumin (*ALB*) promoter (*26*, *37*). The resulting progeny (*Srsf1*$^{flox/+}$ *AlbCre*$^{+/-}$) were mated with *Srsf1*$^{flox/flox}$ mice to generate *Srsf1*$^{flox/flox}$; *AlbCre*$^{+/-}$, or hepatocyte-specific SRSF1 knockout mice (SRSF1 HKO). To generate control mice (*AlbCre*$^{+/-}$), *AlbCre*$^{+/+}$ were mated with wildtype C57BL/6J mice. Genotyping was performed on genomic DNA isolated from tail clipping using primers and protocols described by The Jackson Laboratory. For the acute hepatocyte-specific deletion of SRSF1 (acSRSF1 HKO) mice model, *Srsf1*$^{flox/flox}$ mice were injected with adeno-associated viral vectors (VectorBio Labs) either expressing GFP (Controls) or the Cre recombinase (acSRSF1 HKO) driven by the hepatocyte-specific thyroxine binding globulin (TBG) promoter. Mice were injected at 8 weeks of age with a viral titer of 5 x 10^{11} genome copies (gc) via the tail vein. For the acSRSF1 HKO mice, timepoints are in reference to the time elapsed after viral transduction. Mice were housed on a standard 12-hour-light/dark cycle and were allowed *ad libitum* access to water and a normal chow diet (2918 Envigo Teklad). The mice were fasted for 6 hours prior to harvesting the tissues or blood. National Institutes of Health (NIH) guidelines for the use and care of laboratory animals were followed, and all experiments were approved by the Institutional Animal Care and Use Committee at the University of Illinois at Urbana-Champaign (Champaign, IL).

Blood collection and serum chemistry assays. Mice were fasted about 10 hours prior to blood collection. Blood was collected from the retro-orbital venous sinus using EDTA coated blood collecting capillaries. Mice were temporarily anesthetized using isoflurane before collecting blood. For non-terminal procedures about 200 µL was collected otherwise about 600 µL was collected. Blood from the capillary was transferred into BD microtainer tubes and then centrifuged according

to manufacturer's protocol to separate the serum. Serum was then transferred into 1.5 mL microcentrifuge tubes and snap-frozen in liquid nitrogen before storing at -80 °C. Serum cholesterol, triglycerides, ALT, and AST activity were measured using colorimetric assay kits provided by Infinity (Thermo Scientific). Serum bilirubin, both direct and indirect, was measured using the Sigma Bilirubin Assay kit (MAK126 Sigma) according to the manufacturer's protocol. Snap frozen serum (100 µL) collected from control and acSRSF1 HKO mice were submitted to the Mouse Metabolic Phenotyping Core at the University of Cincinnati for serum analysis. A serum chemistry panel was obtained for each sample with measured concentrations of serum triglycerides, cholesterol, phospholipids, non-esterified fatty acids, glucose, ketones, ALT, and AST.

Histology, immunohistochemistry, and immunofluorescence staining.

Tissue processing and embedding: For paraffin embedding, harvested liver tissue pieces were washed in 1X phosphate buffered saline (PBS) and then immediately fixed in 10% neutral-buffered formalin (NBF) overnight at 4 °C. Fixed tissues were processed through a series of solvents starting from ethanol solutions to xylenes and then embedded into paraffin blocks using standard protocols. For cryo-embedding, washed tissue pieces were positioned into molds containing OCT medium (Tissue-Tek, Sakura) and then frozen using liquid nitrogen.

H&E and Sirius Red staining: Paraffin-embedded tissues sections (5 µm) were cut, placed onto microscope slides, and incubated in a series of xylene and alcohol dilutions to deparaffinize and rehydrate the sections in preparation for further staining. For hematoxylin and eosin (H&E) staining standard procedures were followed using Modified Harris Hematoxylin Solution (7211 Richard-Allan Scientific) and Eosin Y Solution (7111 Richard-Allan Scientific). For Sirius red staining, sections were incubated in Picro-sirius red solution (0.1% w/v Direct Red 80, 365548 Sigma-Aldrich, in a saturated aqueous solution of picric acid) for 1 hour. They were then briefly rinsed in

two changes of 0.5% acetic acid solution. Stained sections were mounted with a coverslip using Permount (SP15-100 Fisher Scientific) mounting media.

Oil red O staining: OCT embedded tissues were sectioned (10 µm) using a cryostat, placed onto a microscope slide, and then fixed in NBF for 15 minutes. Slides were brought to 60% isopropanol solution and then stained with freshly prepared Oil Red O solution (0.3% w/v Oil Red O in 60% isopropanol) for 15 minutes. Once stained, the slides were rinsed in 60% isopropanol solution and gently counterstained with Modified Harris Hematoxylin. Slides were rinsed with distilled water and mounted using CC mount (C9368 Sigma) and coverslip.

Immunohistochemistry (IHC) and immunofluorescent (IF) staining: Paraffin sections were deparaffinized, rehydrated, and then antigen retrieved in Tris-EDTA buffer (10 mM Tris, 1 mM EDTA, 0.05% Tween 20, pH 8.0) using a slow cooker at 120 °C for 10 min. The sections were then incubated in wash buffer containing 1X tris-buffered saline (TBS) and 0.025% Triton X-100 and then blocked using 1X TBS, 10% Normal Goat Serum (NGS) and 1% BSA for 2 hours at room temperature (RT). Primary antibodies were applied to the sections at standardized concentrations and incubated overnight at 4 °C. Next, the sections were washed with wash buffer, and secondary HRP-conjugated or fluorescent antibodies were applied for 1 hour at RT for IHC or IF, respectively. For IHC, sections were washed in 1X TBS and then developed using a DAB Peroxidase Substrate kit (Vector Laboratories) for approximately 5 minutes. Sections were counterstained with hematoxylin, dehydrated into xylenes, and then mounted using Permount. For IF, sections were washed in 1X TBS, stained for the nucleus using ToPro3 (R37170 Thermo Fisher Scientific) for 15 minutes at RT, and then mounted using CC aqueous mounting media. All antibodies used and respective dilutions are listed in Supplementary Table S3.

Imaging and analysis: Histology and IHC slides were imaged on a Hamamatsu Nanozoomer, and IF slides were imaged using a Zeiss LSM 710 microscope at the Institute of Genomic Biology (IGB)

core facility, UIUC. Counting of stained nuclei was performed using built-in thresholding and watershed functions available in Fiji, an open-source image processing program.

Isolation and purification of hepatocytes. Hepatocytes were isolated and purified using the two-step collagenase perfusion technique (*71*). Mice were first anesthetized with isoflurane and then secured to a surgery pad with the ventral side up. A "U" shaped incision was made on the abdomen to expose the liver. The liver was then perfused through the portal vein with 50 ml of wash buffer containing 1X Hanks Balanced Salt Solution (HBSS) and 1 mM EDTA (pH 8.0), without calcium and magnesium salts. Following this, the livers were perfused using 50 ml of digestion buffer containing 1X HBSS, 0.5 mM $CaCl_2$, 40 µg/mL soybean trypsin inhibitor, and 60 U/mL of Collagenase Type I from Worthington. The perfused liver was carefully excised out from the abdomen and transferred into a petri dish containing 1X HBSS. Using cell scrapers, the tissue was carefully massaged to release the cells from the capsule. The crude cell prep was then filtered through a 40 µm mesh filter and the resulting single cell suspension was centrifuged at 50 g for 5 minutes at 4 °C. The supernatant containing non-parenchymal cells and dead hepatocytes was discarded while the pellet containing live hepatocytes were resuspended in fresh 1X HBSS. The centrifugation wash was repeated two additional times before being aliquoted into 1.5 mL microcentrifuge tubes, flash frozen in liquid nitrogen, and stored in -80 °C until further use.

RNA-seq library preparation, sequencing, and analysis. Total RNA was prepared from frozen hepatocyte pellets using the RNeasy tissue mini-kit (Qiagen). Downstream RNA quality was assessed using an Agilent Bioanalyzer and quantified using a Qubit Fluorometer by the Functional Genomic Core at the Roy J. Carver Biotechnology Center, UIUC. Hi-Seq libraries were prepared and 100-bp paired-end Illumina sequencing was performed on a HiSeq 4000 at the High Throughput Sequencing and Genotyping Unit, UIUC. RNA-Seq reads were processed for quality

and read length filters using Trimmomatic (version 0.38) (*72*). For differential gene expression analysis, RNA-Seq reads were psuedoaligned using Kallisto (version 0.44.0) (*73*). Transcript abundances were converted to gene abundances using tximport (version 1.11.7) (*74*). With gene abundance tables, differential gene expression analysis was performed using DESeq2 (version 1.23.10) (*75*). For differential splicing analysis, RNA-Seq reads were trimmed to a set length and then mapped using STAR (version 2.4.2a) onto the mouse vM19 genome (mm10) available from Gencode (https://www.gencodegenes.org) (*76*). Alignment files were then used to perform differential splicing analysis using rMATS (version 3.2.5) and significant events were identified using imposed cutoffs (FDR < 0.10, junction read counts ≥ 10, and deltaPSI ≥ 15%) (*77*). Gene ontology analysis was performed using gProfiler and Enrichr (*78*, *79*). Filtering and processing of data was performed using custom Python and R Scripts. Details regarding RNA-seq sample information are provided in Supplementary Table S6.

Protein isolation and western blot analysis. Total proteins were isolated from ~50 mg of snap frozen liver tissue or purified cell pellet by homogenizing in 400 µL of cold homogenization buffer containing 10 mM HEPES (pH 7.5), 0.32M Sucrose, 5 mM EDTA, 1% SDS, 5 µM MG132 and Pierce Protease Inhibitors (1 tablet per 10 mL of buffer, Catalog # A32953). Samples were sonicated in a water bath to shear DNA and clarified by centrifugation. Protein concentration was determined using the Pierce™ BCA Protein Assay Kit (Thermo Scientific). Protein lysates were diluted to 5 mg/mL and then boiled in 1X Laemmli buffer at 100 °C for 10 minutes. For cultured cells, samples were directly lysed in 2X Laemmli buffer (200 µL/well for 6-well plate), sonicated, and then boiled. After boiling, samples were cooled to room temperature and ~50 µg of proteins were resolved on a 10% SDS-PAGE gel and transferred using a wet transfer setup onto a PVDF membrane with 0.45 µm pore size (Immobilon, Millipore). Membranes were blocked using Tris-buffered saline containing 5% nonfat dry milk and 0.1% Tween 20 (TBST). After blocking,

667 membranes were incubated with primary antibody overnight at 4°C. The membranes were then
668 washed with TBST to remove any unbound primary antibody followed by incubation with an
669 appropriate horseradish peroxidase-conjugated secondary antibody for two hours. Membranes went
670 through a final TBST wash and then visualized on the ChemiDoc XRS+ using the Clarity Western
671 ECL kit (BioRad).
672
673 **Hepatic lipid isolation and quantification.** Lipids were extracted from approximately 100 mg of
674 liver tissue using the Folch Method (*80*). Briefly, the tissue was homogenized in 1 mL of 2:1
675 choroform:methanol mixture. The homogenized mixture was incubated overnight at room
676 temperature to allow for complete extraction. The mixture was then centrifuged at 10,000 x g for
677 10 minutes to pellet any debris. The supernatant was transferred to a fresh tube. The interface was
678 washed with 1 X PBS solution to remove any additional salt. The mixture was centrifuged at 4,000
679 x g and aqueous layer was removed. The organic phase was dried under nitrogen stream and then
680 reconstituted in 300 µL of ethanol. The reconstituted mixture was used with Infinity Kit to
681 determine concentrations of triglycerides and cholesterol.
682
683 **Global proteomics analysis by mass spectrometry.** Samples were processed for proteomics
684 according to the FASP protocol and desalted on an in-house prepared C18 tips (*81*). The peptides
685 were separated on an EASY Spray C18 column (50 cm x 75 cm, 2 µm particle size) (ThermoFisher
686 Scientific, Toronto) using an EASY nLC-1200. The mobile phase was composed of 0.1% formic
687 acid in water (A) and 80% acetonitrile with 0.1% formic acid (B). The gradient was as follows: 5 -
688 40% B (0 – 120 minutes), 40% - 100% B (120 – 125 minutes), 100% B (125 – 135 minutes). The
689 peptides were analyzed on a Thermo QExactive HF mass spectrometer in a Top 20 data dependent
690 acquisition mode. Proteins were identified using MaxQuant to search the mouse (UP000000589)
691 proteomes from UniProtKB (February 2019). Peptide spectral matches, and protein False

692 Discovery Rates were set to 1%, and requiring a minimum of 1 unique peptide for identification.
693 To increase the number of identified matches, match between runs was enabled with a match time
694 window of 0.7 minutes. Protein abundances were calculated using the iBAQ algorithm in
695 MaxQuant. Differential protein abundance was performed using student's t-test with Bonferroni
696 correction on iBAQ values between control and acSRSF1 HKO.
697
698 **Global translation quantification by SUnSET assay.** Translating proteins were labeled using a
699 protocol adapted from the Surface Sensing of Translation (SUnSET) method (*52*). Mice were
700 injected with puromycin prepared in sterile PBS with a dosage of 0.04 µmol per gram body weight.
701 After 45 minutes, livers were harvested, and protein lysates were prepared as described previously.
702 Proteins were separated by 10% SDS-PAGE and then transferred onto a PVDF membrane.
703 Puromycin-labeled peptides were identified using the mouse monoclonal antibody 12D10 (EMD
704 Millipore Catalog# MABE343). Relative protein synthesis levels were determined by densitometry
705 analysis of whole lanes.
706
707 **Dot blot assays for DNA-RNA hybrid and polyA mRNA**. DNA-RNA hybrid dot blot assay was
708 adapted from a previously published report (*82*). Briefly, DNA was isolated from approximately 50
709 mg of liver tissue or snap frozen cells using DNeasy Blood & Tissue Kit (Qiagen) using the
710 manufacturer's protocol. For each sample 250 ng of DNA was digested with 5 Units of RNase H
711 (NEB) as control. A slot blot apparatus was used to dot blot 250 ng of DNA onto a Hybond^{TM}-N+
712 membrane (Amersham). The membrane was auto cross-linked with UV (254 nm, 1200 mJ/cm^2). It
713 was then air-dried before beginning blocking with 5% nonfat dry milk and 0.1% Tween 20 (TBST)
714 at RT for 30 minutes. Membrane was then incubated overnight at 4°C with S9.6 antibody diluted
715 in blocking buffer. Finally, it was probed with HRP-conjugated anti-mouse secondary antibody,

washed with TBST, and visualized on the ChemiDoc XRS+ using the Clarity Western ECL kit (BioRad). All antibodies used and respective dilutions are listed in *Supplementary Table 3*.

Dot blot analysis for polyA mRNA was performed on total RNA to indirectly assess relative activity of global transcription. Total RNA was isolated from approximately 50 mg of snap frozen liver tissue using the RNeasy kit following standard protocols. 250 ng of total RNA was blotted onto membrane as described previously for DNA-RNA hybrid assay. Membrane was UV crosslinked and air dried before continuing. The blot was prehybridized with ULTRAhyb-Oligo Hybridization Buffer (Thermo Fisher Scientific) for 10 minutes at 42 °C with gentle agitation in a hybridization oven. PolyA mRNA was detected using biotinylated oligo-dT probes (Promega #Z5261). Probe was diluted in ULTRAhyb-Oligo Hybridization Buffer (0.5 µL of 5 pmol/uL per mL of buffer). Blot was incubated with probe solution at 42 °C for 1 hour. Blot was then washed twice with ULTRAhyb-Oligo Hybridization Buffer. Chemiluminescent detection was performed using the Chemiluminescent Nucleic Acid Detection Module Kit (Thermo Fisher Scientific # 89880) following manufacturers protocol.

Cell culture and siRNA knockdown experiments. HepG2 cell line was obtained from ATCC (catalog HB-8065) and cultured according to ATCC specifications. Cells were cultured in DMEM supplemented with 10% FBS, 2 mM glutamine, and 10 U/ml penicillin and streptomycin. For knockdown experiments silencer select siRNAs against *SRSF1 and TP53* (Thermo Fisher Scientific #4392420 and #4390824) along with a negative control (Thermo Fisher Scientific #4390843) were used. Approximately 500,00 cells were seeded into a 6-well format and were reverse transfected with 20 nM of gene-specific siRNA oligos using RNAiMax (Thermo Fisher Scientific #13778075) and then transfected again after 24 hours using forward transfection with 20 nM of siRNA. Cells were harvested at either 36 or 48 hours starting from the initial reverse transfection. For end-point assays requiring fluorescent imaging, cells were grown on coverslips coated with poly-L-lysine,

740 0.1% (w/v) (Sigma-Aldrich #P8920). Detailed protocols on immunofluorescent assays performed
741 on the cultured cells are available in Supplementary Materials.
742
743 **Statistical analysis and data visualization.** All quantitative measurements (i.e., weights, serum
744 assays, western blots) have at least three independent biological repeats. The results were expressed
745 with mean and standard deviation, unless mentioned otherwise. Differences between groups were
746 examined for statistical significance using unpaired t-test with Welch's correction (for two groups),
747 or one-way ANOVA for more than two groups using core functions available in R, an open-source
748 statistical computing software environment. P-value < 0.05 or FDR < 0.10 was considered
749 significant. All data plots were generated in R using the ggplot2 package. Heatmaps were created
750 using the heatmap.2 function available in the gplots package in R. The gene ontology network map
751 was created using Cytoscape 3.8.0 (*83*).

Acknowledgments: We thank the members of the Kalsotra and Anakk laboratories for their valuable discussions and comments on the manuscript.

Funding: This research was supported through the NIH grants R01AA010154, R01HL126845, and R21HD104039 (to A.K.), R01DK113080 (to S.A.), R01GM132458 and R21AG065748, (to K.V.P.), and R01HG004659, U41HG009889 (to G.W.Y.); the William C. Rose Professorship and the Beckman Fellowship from the Center for Advanced Study at the University of Illinois (to A.K.); Natural Sciences and Engineering Research Council of Canada grant RGPIN-2020-07212 (to C.L.C.); Cancer center @ Illinois seed grants (to A.K, K.V.P, and S.A); the American Cancer Society grant RSG ACS132640 (to S.A.); the NSF grant MCB1723008 (to K.V.P.); the NIH pre-doctoral NRSA fellowship F30DK108567 (to W.A.); the NIH Tissue microenvironment training program T32-EB019944 and UIUC Scott Dissertation Fellowship (to S.B.); and the Ontario Graduate Scholarship (to M.F.S.).

Author contributions: W.A. and A.K. conceived the project and designed the experiments. W.A. performed all experiments and analyzed the data. B.M. performed qPCRs and assisted with tissue harvesting and animal studies. M.F.S. and C.L.C. performed mass spectrometry and differential proteomics analysis. S.M.B., B.A.Y. and E.V.N. performed eCLIP experiments and peak calling analysis. G.W.Y. supervised eCLIP experiments. U.V.C., S.B., and Q.H. assisted with cell culture, protein synthesis and western blot experiments. W.A. and A.K. interpreted results and wrote the manuscript. All authors discussed results and edited the manuscript.

Declaration of Interests: G.W.Y is co-founder, member of the Board of Directors, on the scientific advisory boards, equity holder, and paid consultant for Locanabio and Eclipse BioInnovations. G.W.Y is a visiting professor at the National University of Singapore. G.W.Y's interest(s) have been reviewed and approved by the University of California, San Diego in accordance with its conflict-of-interest policies. E.V.N is co-founder, member of the Board of Directors, on the SAB, equity holder, and paid consultant for Eclipse BioInnovations. E.V.N's interests have been

777 reviewed and approved by the University of California, San Diego in accordance with its conflict
778 of interest policies. The authors declare no other competing financial interests.

779 **Data and materials availability:** The raw RNA-seq data are available for download from NCBI
780 Gene Expression Omnibus (http://www.ncbi.nlm.nih.gov/geo/) under the accession numbers
781 GSE147005 and GSE179634. The mass spectrometry proteomics data were deposited to the
782 ProteomeXchange Consortium (http://proteomecentral.proteomexchange.org) via the PRIDE
783 partner repository with the dataset identifier (PXD027035). All data needed to evaluate the
784 conclusions in the paper are present in the paper and/or the Supplementary Materials.

785

References

1. R. Gebhardt, Metabolic zonation of the liver: Regulation and implications for liver function. *Pharmacol. Ther.* **53** (1992), pp. 275–354.

2. J. Galgani, E. Ravussin, Energy metabolism, fuel selection and body weight regulation. *Int. J. Obes.* **32** (2008), pp. 109–119.

3. M. Asrih, F. R. Jornayvaz, Metabolic syndrome and nonalcoholic fatty liver disease: Is insulin resistance the link? *Mol. Cell. Endocrinol.* **418** (2015), pp. 55–65.

4. S. K. Asrani, H. Devarbhavi, J. Eaton, P. S. Kamath, Burden of liver diseases in the world. *J. Hepatol.* **70** (2019), pp. 151–171.

5. S. A. Harrison, S. Gawrieh, K. Roberts, C. J. Lisanti, R. B. Schwope, K. M. Cebe, V. Paradis, P. Bedossa, J. M. Aldridge Whitehead, A. Labourdette, V. Miette, S. Neubauer, C. Fournier, A. H. Paredes, N. Alkhouri, Prospective evaluation of the prevalence of non-alcoholic fatty liver disease and steatohepatitis in a large middle-aged US cohort. *J. Hepatol.* (2021), doi:10.1016/j.jhep.2021.02.034.

6. X. Zhang, M. Wu, Z. Liu, H. Yuan, X. Wu, T. Shi, X. Chen, T. Zhang, Increasing prevalence of nafld/nash among children, adolescents and young adults from 1990 to 2017: A population-based observational study. *BMJ Open*. **11** (2021), pp. e042843–e042843.

7. A. M. Diehl, N. J. Farpour-Lambert, L. Zhao, H. Tilg, Why we need to curb the emerging worldwide epidemic of nonalcoholic fatty liver disease. *Nat. Metab.* **1** (2019), pp. 1027–1029.

8. E. E. Powell, V. W. S. Wong, M. Rinella, Non-alcoholic fatty liver disease. *Lancet*. **397** (2021), pp. 2212–2224.

9. A. Bhate, D. J. Parker, T. W. Bebee, J. Ahn, W. Arif, E. H. Rashan, S. Chorghade, A. Chau, J.-H. Lee, S. Anakk, R. P. Carstens, X. Xiao, A. Kalsotra, ESRP2 controls an adult splicing programme in hepatocytes to support postnatal liver maturation. *Nat. Commun.* **6**,

8768 (2015).

10. S. Bangru, W. Arif, J. Seimetz, A. Bhate, J. Chen, E. H. Rashan, R. P. Carstens, S. Anakk, A. Kalsotra, Alternative splicing rewires Hippo signaling pathway in hepatocytes to promote liver regeneration. *Nat. Struct. Mol. Biol.* **25**, 928–939 (2018).

11. M. Elizalde, R. Urtasun, M. Azkona, M. U. Latasa, S. Goñi, O. García-Irigoyen, I. Uriarte, V. Segura, M. Collantes, M. Di Scala, A. Lujambio, J. Prieto, M. A. Ávila, C. Berasain, Splicing regulator SLU7 is essential for maintaining liver homeostasis. *J. Clin. Invest.* **124**, 2909–2920 (2014).

12. G. Benegiamo, L. S. Mure, G. Erikson, H. D. Le, E. Moriggi, S. A. Brown, S. Panda, The RNA-Binding Protein NONO Coordinates Hepatic Adaptation to Feeding. *Cell Metab.* **27**, 404-418.e7 (2018).

13. K. C. Nikolaou, H. Vatandaslar, C. Meyer, M. W. Schmid, T. Tuschl, M. Stoffel, The RNA-Binding Protein A1CF Regulates Hepatic Fructose and Glycerol Metabolism via Alternative RNA Splicing. *Cell Rep.* **29**, 283-300.e8 (2019).

14. J. Hyun, Z. Sun, A. R. Ahmadi, S. Bangru, U. V. Chembazhi, K. Du, T. Chen, H. Tsukamoto, I. Rusyn, A. Kalsotra, A. M. Diehl, Epithelial splicing regulatory protein 2-mediated alternative splicing reprograms hepatocytes in severe alcoholic hepatitis. *J. Clin. Invest.* **130**, 2129–2145 (2020).

15. A. H. Corbett, Post-transcriptional regulation of gene expression and human disease. *Curr. Opin. Cell Biol.* **52** (2018), pp. 96–104.

16. B. S. Zhao, I. A. Roundtree, C. He, Post-transcriptional gene regulation by mRNA modifications. *Nat. Rev. Mol. Cell Biol.* **18** (2016), pp. 31–42.

17. W. Arif, G. Datar, A. Kalsotra, Intersections of post-transcriptional gene regulatory mechanisms with intermediary metabolism. *Biochim. Biophys. Acta - Gene Regul. Mech.* **1860**, 349–362 (2017).

836 18. J. M. Howard, J. R. Sanford, THE RNAissance Family: SR proteins as multifaceted
837 regulators of gene expression. *Wiley Interdiscip Rev RNA*. **6**, 93–110 (2015).
838 19. Y. Cheng, C. Luo, W. Wu, Z. Xie, X. Fu, Y. Feng, Liver-Specific Deletion of SRSF2
839 Caused Acute Liver Failure and Early Death in Mice. *Mol. Cell. Biol.* **36**, 1628–1638
840 (2016).
841 20. S. Sen, H. Jumaa, N. J. G. Webster, Splicing factor SRSF3 is crucial for hepatocyte
842 differentiation and metabolic function. *Nat. Commun.* **4**, 1336 (2013).
843 21. J. Pihlajamäki, C. Lerin, P. Itkonen, T. Boes, T. Floss, J. Schroeder, F. Dearie, S.
844 Crunkhorn, F. Burak, J. C. Jimenez-Chillaron, T. Kuulasmaa, P. Miettinen, P. J. Park, I.
845 Nasser, Z. Zhao, Z. Zhang, Y. Xu, W. Wurst, H. Ren, A. J. Morris, S. Stamm, A. B.
846 Goldfine, M. Laakso, M. E. Patti, Expression of the splicing factor gene SFRS10 is
847 reduced in human obesity and contributes to enhanced lipogenesis. *Cell Metab.* **14**, 208–
848 218 (2011).
849 22. M. Müller-McNicoll, V. Botti, A. M. de Jesus Domingues, H. Brandl, O. D. Schwich, M.
850 C. Steiner, T. Curk, I. Poser, K. Zarnack, K. M. Neugebauer, SR proteins are NXF1
851 adaptors that link alternative RNA processing to mRNA export. *Genes Dev.* (2016),
852 doi:10.1101/gad.276477.115.
853 23. M. M. Maslon, S. R. Heras, N. Bellora, E. Eyras, J. F. Cáceres, The translational landscape
854 of the splicing factor SRSF1 and its role in mitosis. *Elife*. **2014**, e02028 (2014).
855 24. S. Das, A. R. Krainer, Emerging Functions of SRSF1, Splicing Factor and Oncoprotein, in
856 RNA Metabolism and Cancer (2014), doi:10.1158/1541-7786.MCR-14-0131.
857 25. X. Li, J. L. Manley, Inactivation of the SR protein splicing factor ASF/SF2 results in
858 genomic instability. *Cell*. **122**, 365–378 (2005).
859 26. X. Xu, D. Yang, J.-H. Ding, W. Wang, P.-H. Chu, N. D. Dalton, H.-Y. Wang, J. R.
860 Bermingham, Z. Ye, F. Liu, M. G. Rosenfeld, J. L. Manley, J. Ross, J. Chen, R.-P. Xiao,

H. Cheng, X.-D. Fu, ASF/SF2-regulated CaMKIIdelta alternative splicing temporally reprograms excitation-contraction coupling in cardiac muscle. *Cell*. **120**, 59–72 (2005).

27. T. Katsuyama, H. Li, D. Comte, G. C. Tsokos, V. R. Moulton, Splicing factor SRSF1 controls T cell hyperactivity and systemic autoimmunity. *J. Clin. Invest.* **129**, 5411–5423 (2019).

28. T. Katsuyama, I. J. Martin-Delgado, S. M. Krishfield, V. C. Kyttaris, V. R. Moulton, Splicing factor SRSF1 controls T cell homeostasis and its decreased levels are linked to lymphopenia in systemic lupus erythematosus. *Rheumatol. (United Kingdom)*. **59**, 2146–2155 (2020).

29. Z. Qi, F. Wang, G. Yu, D. Wang, Y. Yao, M. You, J. Liu, J. Liu, Z. Sun, C. Ji, Y. Xue, S. Yu, SRSF1 serves as a critical posttranscriptional regulator at the late stage of thymocyte development. *Sci. Adv.* **7**, 753–769 (2021).

30. N. Xie, M. Chen, R. Dai, Y. Zhang, H. Zhao, Z. Song, L. Zhang, Z. Li, Y. Feng, H. Gao, L. Wang, T. Zhang, R. P. Xiao, J. Wu, C. M. Cao, SRSF1 promotes vascular smooth muscle cell proliferation through a Δ133p53/EGR1/KLF5 pathway. *Nat. Commun.* **8**, 16016 (2017).

31. Y. Liu, Y. Luo, L. Shen, R. Guo, Z. Zhan, N. Yuan, R. Sha, W. Qian, Z. Wang, Z. Xie, W. Wu, Y. Feng, Splicing Factor SRSF1 Is Essential for Satellite Cell Proliferation and Postnatal Maturation of Neuromuscular Junctions in Mice. *Stem Cell Reports*. **15**, 941–954 (2020).

32. R. Karni, E. De Stanchina, S. W. Lowe, R. Sinha, D. Mu, A. R. Krainer, The gene encoding the splicing factor SF2/ASF is a proto-oncogene. *Nat. Struct. Mol. Biol.* **14**, 185–193 (2007).

33. O. I. Fregoso, S. Das, M. Akerman, A. R. Krainer, Splicing-Factor Oncoprotein SRSF1 Stabilizes p53 via RPL5 and Induces Cellular Senescence. *Mol. Cell*. **50**, 56–66 (2013).

886 34. L. Chen, C. Luo, L. Shen, Y. Liu, Q. Wang, C. Zhang, R. Guo, Y. Zhang, Z. Xie, N. Wei,
887 W. Wu, J. Han, Y. Feng, SRSF1 Prevents DNA Damage and Promotes Tumorigenesis
888 through Regulation of DBF4B Pre-mRNA Splicing. *Cell Rep.* **21**, 3406–3413 (2017).
889 35. O. Anczuków, A. Z. Rosenberg, M. Akerman, S. Das, L. Zhan, R. Karni, S. K.
890 Muthuswamy, A. R. Krainer, The splicing factor SRSF1 regulates apoptosis and
891 proliferation to promote mammary epithelial cell transformation. *Nat. Struct. Mol. Biol.* **19**,
892 220–8 (2012).
893 36. O. Anczuków, M. Akerman, A. Cléry, J. Wu, C. Shen, N. H. Shirole, A. Raimer, S. Sun,
894 M. A. Jensen, Y. Hua, F. H. T. Allain, A. R. Krainer, SRSF1-Regulated Alternative
895 Splicing in Breast Cancer. *Mol. Cell*. **60**, 105–117 (2015).
896 37. C. Postic, M. Shiota, K. D. Niswender, T. L. Jetton, Y. Chen, J. M. Moates, K. D. Shelton,
897 J. Lindner, A. D. Cherrington, M. A. Magnuson, Dual Roles for Glucokinase in Glucose
898 Homeostasis as Determined by Liver and Pancreatic β Cell-specific Gene Knock-outs
899 Using Cre Recombinase. *J. Biol. Chem.* **274**, 305–315 (1999).
900 38. C. M. Weisend, J. A. Kundert, E. S. Suvorova, J. R. Prigge, E. E. Schmidt, Cre activity in
901 fetal albCre mouse hepatocytes: Utility for developmental studies. *Genesis*. **47**, 789–792
902 (2009).
903 39. S. Sekine, R. Ogawa, R. Ito, N. Hiraoka, M. T. McManus, Y. Kanai, M. Hebrok,
904 Disruption of Dicer1 Induces Dysregulated Fetal Gene Expression and Promotes
905 Hepatocarcinogenesis. *Gastroenterology*. **136**, 2304-2315.e4 (2009).
906 40. C. C. Duwaerts, J. J. Maher, Mechanisms of Liver Injury in Non-Alcoholic Steatohepatitis.
907 *Curr. Hepatol. reports*. **13**, 119–129 (2014).
908 41. E. M. Brunt, D. E. Kleiner, L. a. Wilson, P. Belt, B. a. Neuschwander-Tetri, Nonalcoholic
909 fatty liver disease (NAFLD) activity score and the histopathologic diagnosis in NAFLD:
910 Distinct clinicopathologic meanings. *Hepatology*. **53**, 810–820 (2011).

911 42. M. T. Lovci, D. Ghanem, H. Marr, J. Arnold, S. Gee, M. Parra, T. Y. Liang, T. J. Stark, L.
912 T. Gehman, S. Hoon, K. B. Massirer, G. A. Pratt, D. L. Black, J. W. Gray, J. G. Conboy,
913 G. W. Yeo, Rbfox proteins regulate alternative mRNA splicing through evolutionarily
914 conserved RNA bridges. *Nat. Struct. Mol. Biol.* **20**, 1434–1442 (2013).
915 43. H. Sato, N. Hosoda, L. E. Maquat, Efficiency of the Pioneer Round of Translation Affects
916 the Cellular Site of Nonsense-Mediated mRNA Decay. *Mol. Cell*. **29**, 255–262 (2008).
917 44. Z. Zhang, A. R. Krainer, Involvement of SR proteins in mRNA surveillance. *Mol. Cell*. **16**,
918 597–607 (2004).
919 45. L. Dara, C. Ji, N. Kaplowitz, The contribution of endoplasmic reticulum stress to liver
920 diseases. *Hepatology*. **53**, 1752–1763 (2011).
921 46. C. M. Oslowski, F. Urano, *Measuring ER stress and the unfolded protein response using*
922 *mammalian tissue culture system.* (Elsevier Inc., ed. 1, 2011;
923 http://www.pubmedcentral.nih.gov/articlerender.fcgi?artid=3701721&tool=pmcentrez&ren
924 dertype=abstract), vol. 490.
925 47. A. Samali, U. Fitzgerald, S. Deegan, S. Gupta, Methods for monitoring endoplasmic
926 reticulum stress and the unfolded protein response. *Int. J. Cell Biol.* **2010**, 830307 (2010).
927 48. J. M. Santos-Pereira, A. Aguilera, R loops: New modulators of genome dynamics and
928 function. *Nat. Rev. Genet.* **16** (2015), pp. 583–597.
929 49. L. J. Mah, A. El-Osta, T. C. Karagiannis, γh2AX: A sensitive molecular marker of DNA
930 damage and repair. *Leukemia*. **24** (2010), pp. 679–686.
931 50. G. Michlewski, J. R. Sanford, J. F. Cáceres, The Splicing Factor SF2/ASF Regulates
932 Translation Initiation by Enhancing Phosphorylation of 4E-BP1. *Mol. Cell*. **30**, 179–189
933 (2008).
934 51. J. R. Sanford, N. K. Gray, K. Beckmann, J. F. Cáceres, A novel role for shuttling SR
935 proteins in mRNA translation. *Genes Dev.* **18**, 755–768 (2004).

52. C. A. Goodman, T. A. Hornberger, Measuring protein synthesis with SUnSET: a valid alternative to traditional techniques? *Exerc. Sport Sci. Rev.* **41**, 107–15 (2013).

53. B. F. Teske, S. A. Wek, P. Bunpo, J. K. Cundiff, J. N. McClintick, T. G. Anthony, R. C. Wek, The eIF2 kinase PERK and the integrated stress response facilitate activation of ATF6 during endoplasmic reticulum stress. *Mol. Biol. Cell*. **22**, 4390–4405 (2011).

54. A. W. Wang, K. J. Wangensteen, Y. J. Wang, A. M. Zahm, N. G. Moss, N. Erez, K. H. Kaestner, TRAP-seq identifies cystine/glutamate antiporter as a driver of recovery from liver injury. *J. Clin. Invest.* **128**, 2297–2309 (2018).

55. U. V. Chembazhi, S. Bangru, M. Hernaez, A. Kalsotra, Cellular plasticity balances the metabolic and proliferation dynamics of a regenerating liver. *Genome Res.* **31**, 576–591 (2021).

56. D. Westphal, G. Dewson, P. E. Czabotar, R. M. Kluck, Molecular biology of Bax and Bak activation and action. *Biochim. Biophys. Acta - Mol. Cell Res.* **1813** (2011), pp. 521–531.

57. L. Duprez, N. Takahashi, F. Van Hauwermeiren, B. Vandendriessche, V. Goossens, T. Vanden Berghe, W. Declercq, C. Libert, A. Cauwels, P. Vandenabeele, RIP Kinase-Dependent Necrosis Drives Lethal Systemic Inflammatory Response Syndrome. *Immunity*. **35**, 908–918 (2011).

58. M. Pasparakis, P. Vandenabeele, Necroptosis and its role in inflammation. *Nature*. **517** (2015), pp. 311–320.

59. B. Sundararaman, L. Zhan, S. M. Blue, R. Stanton, K. Elkins, S. Olson, X. Wei, E. L. Van Nostrand, G. A. Pratt, S. C. Huelga, B. M. Smalec, X. Wang, E. L. Hong, J. M. Davidson, E. Lécuyer, B. R. Graveley, G. W. Yeo, Resources for the Comprehensive Discovery of Functional RNA Elements. *Mol. Cell*. **61**, 903–913 (2016).

60. M. Wade, Y. C. Li, G. M. Wahl, MDM2, MDMX and p53 in oncogenesis and cancer therapy. *Nat. Rev. Cancer*. **13** (2013), pp. 83–96.

961 61. K. T. Bieging, L. D. Attardi, Deconstructing p53 transcriptional networks in tumor
962 suppression. *Trends Cell Biol.* **22** (2012), pp. 97–106.
963 62. J. C. Long, J. F. Caceres, The SR protein family of splicing factors: master regulators of
964 gene expression. *Biochem. J.* **417**, 15–27 (2009).
965 63. A. W. Duncan, A. E. Hanlon Newell, W. Bi, M. J. Finegold, S. B. Olson, A. L. Beaudet,
966 M. Grompe, Aneuploidy as a mechanism for stress-induced liver adaptation. *J. Clin. Invest.*
967 **122**, 3307–3315 (2012).
968 64. A. W. Duncan, Aneuploidy, polyploidy and ploidy reversal in the liver. *Semin. Cell Dev.*
969 *Biol.* **24** (2013), pp. 347–356.
970 65. P. D. Wilkinson, F. Alencastro, E. R. Delgado, M. P. Leek, M. P. Weirich, P. A. Otero, N.
971 Roy, W. K. Brown, M. Oertel, A. W. Duncan, Polyploid Hepatocytes Facilitate Adaptation
972 and Regeneration to Chronic Liver Injury. *Am. J. Pathol.* **189**, 1241–1255 (2019).
973 66. M. Jiménez, R. Urtasun, M. Elizalde, M. Azkona, M. U. Latasa, I. Uriarte, M. Arechederra,
974 D. Alignani, M. Bárcena-Varela, G. Álvarez-Sola, L. Colyn, E. Santamaría, B. Sangro, C.
975 Rodriguez-Ortigosa, M. G. Fernández-Barrena, M. A. Ávila, C. Berasain, Splicing events
976 in the control of genome integrity: role of SLU7 and truncated SRSF3 proteins. *Nucleic*
977 *Acids Res.* **47**, 3450–3466 (2019).
978 67. V. O. Wickramasinghe, A. R. Venkitaraman, RNA Processing and Genome Stability:
979 Cause and Consequence. *Mol. Cell*. **61** (2016), pp. 496–505.
980 68. B. Gómez-González, M. García-Rubio, R. Bermejo, H. Gaillard, K. Shirahige, A. Marín,
981 M. Foiani, A. Aguilera, Genome-wide function of THO/TREX in active genes prevents R-
982 loop-dependent replication obstacles. *EMBO J.* **30**, 3106–3119 (2011).
983 69. L. Wahba, J. D. Amon, D. Koshland, M. Vuica-Ross, RNase H and Multiple RNA
984 Biogenesis Factors Cooperate to Prevent RNA:DNA Hybrids from Generating Genome
985 Instability. *Mol. Cell*. **44**, 978–988 (2011).

70. R. D. Paulsen, D. V. Soni, R. Wollman, A. T. Hahn, M. C. Yee, A. Guan, J. A. Hesley, S. C. Miller, E. F. Cromwell, D. E. Solow-Cordero, T. Meyer, K. A. Cimprich, A Genome-wide siRNA Screen Reveals Diverse Cellular Processes and Pathways that Mediate Genome Stability. *Mol. Cell*. **35**, 228–239 (2009).

71. W. C. Li, K. L. Ralphs, D. Tosh, Isolation and culture of adult mouse hepatocytes. *Methods Mol. Biol.* (2010), doi:10.1007/978-1-59745-019-5_13.

72. A. M. Bolger, M. Lohse, B. Usadel, Genome analysis Trimmomatic: a flexible trimmer for Illumina sequence data. **30**, 2114–2120 (2014).

73. N. L. Bray, H. Pimentel, P. Melsted, L. Pachter, Near-optimal probabilistic RNA-seq quantification. *Nat. Biotechnol.* **34**, 525–527 (2016).

74. C. Soneson, M. I. Love, M. D. Robinson, Differential analyses for RNA-seq: transcript-level estimates improve gene-level inferences. *F1000Research*. **4**, 1521 (2015).

75. M. I. Love, W. Huber, S. Anders, Moderated estimation of fold change and dispersion for RNA-seq data with DESeq2. *Genome Biol.* **15**, 550 (2014).

76. A. Dobin, C. A. Davis, F. Schlesinger, J. Drenkow, C. Zaleski, S. Jha, P. Batut, M. Chaisson, T. R. Gingeras, Sequence analysis STAR: ultrafast universal RNA-seq aligner. **29**, 15–21 (2013).

77. S. Shen, J. W. Park, Z. X. Lu, L. Lin, M. D. Henry, Y. N. Wu, Q. Zhou, Y. Xing, rMATS: Robust and flexible detection of differential alternative splicing from replicate RNA-Seq data. *Proc. Natl. Acad. Sci. U. S. A.* **111**, E5593–E5601 (2014).

78. U. Raudvere, L. Kolberg, I. Kuzmin, T. Arak, P. Adler, H. Peterson, J. Vilo, G:Profiler: A web server for functional enrichment analysis and conversions of gene lists (2019 update). *Nucleic Acids Res.* **47**, W191–W198 (2019).

79. M. V Kuleshov, M. R. Jones, A. D. Rouillard, N. F. Fernandez, Q. Duan, Z. Wang, S. Koplev, S. L. Jenkins, K. M. Jagodnik, A. Lachmann, M. G. McDermott, C. D. Monteiro,

1011 G. W. Gundersen, A. Ma'ayan, Enrichr: a comprehensive gene set enrichment analysis web
1012 server 2016 update. *Nucleic Acids Res.* **44**, W90–W97 (2016).
1013 80. J. Folch, M. Lees, G. H. Sloane, A simple method for the isolation and purification of total
1014 lipides from animal tissues. *J. Biol. Chem.* **226**, 497–509 (1957).
1015 81. J. R. Wiśniewski, A. Zougman, N. Nagaraj, M. Mann, Universal sample preparation
1016 method for proteome analysis. *Nat. Methods*. **6**, 359–362 (2009).
1017 82. J. C. Morales, P. Richard, P. L. Patidar, E. A. Motea, T. T. Dang, J. L. Manley, D. A.
1018 Boothman, XRN2 Links Transcription Termination to DNA Damage and Replication
1019 Stress. *PLoS Genet.* **12** (2016), doi:10.1371/journal.pgen.1006107.
1020 83. P. Shannon, A. Markiel, O. Ozier, N. S. Baliga, J. T. Wang, D. Ramage, N. Amin, B.
1021 Schwikowski, T. Ideker, Cytoscape : A Software Environment for Integrated Models of
1022 Biomolecular Interaction Networks Cytoscape : A Software Environment for Integrated
1023 Models of Biomolecular Interaction Networks, 2498–2504 (2003).
1024 84. E. L. Van Nostrand, G. A. Pratt, A. A. Shishkin, C. Gelboin-Burkhart, M. Y. Fang, B.
1025 Sundararaman, S. M. Blue, T. B. Nguyen, C. Surka, K. Elkins, R. Stanton, F. Rigo, M.
1026 Guttman, G. W. Yeo, Robust transcriptome-wide discovery of RNA-binding protein
1027 binding sites with enhanced CLIP (eCLIP). *Nat. Methods*. **13**, 508–514 (2016).
1028 85. E. L. Van Nostrand, P. Freese, G. A. Pratt, X. Wang, X. Wei, R. Xiao, S. M. Blue, J. Y.
1029 Chen, N. A. L. Cody, D. Dominguez, S. Olson, B. Sundararaman, L. Zhan, C. Bazile, L. P.
1030 B. Bouvrette, J. Bergalet, M. O. Duff, K. E. Garcia, C. Gelboin-Burkhart, M. Hochman, N.
1031 J. Lambert, H. Li, M. P. McGurk, T. B. Nguyen, T. Palden, I. Rabano, S. Sathe, R. Stanton,
1032 A. Su, R. Wang, B. A. Yee, B. Zhou, A. L. Louie, S. Aigner, X. D. Fu, E. Lécuyer, C. B.
1033 Burge, B. R. Graveley, G. W. Yeo, A large-scale binding and functional map of human
1034 RNA-binding proteins. *Nature*. **583**, 711–719 (2020).
1035 86. T. L. Bailey, STREME: accurate and versatile sequence motif discovery. *Bioinformatics*

(2021), doi:10.1093/bioinformatics/btab203.

87. B. A. Yee, G. A. Pratt, B. R. Graveley, E. L. van Nostrand, G. W. Yeo, RBP-Maps enables robust generation of splicing regulatory maps. *RNA*. **25**, 193–204 (2019).

88. J. Seimetz, W. Arif, S. Bangru, M. Hernaez, A. Kalsotra, Cell-type specific polysome profiling from mammalian tissues. *Methods*. **155**, 131–139 (2019).

89. P. S. Aranda, D. M. LaJoie, C. L. Jorcyk, Bleach gel: a simple agarose gel for analyzing RNA quality. *Electrophoresis*. **33**, 366–9 (2012).

90. K. J. Livak, T. D. Schmittgen, Analysis of relative gene expression data using real-time quantitative PCR and the 2-ΔΔCT method. *Methods*. **25**, 402–408 (2001).

Figures and Tables

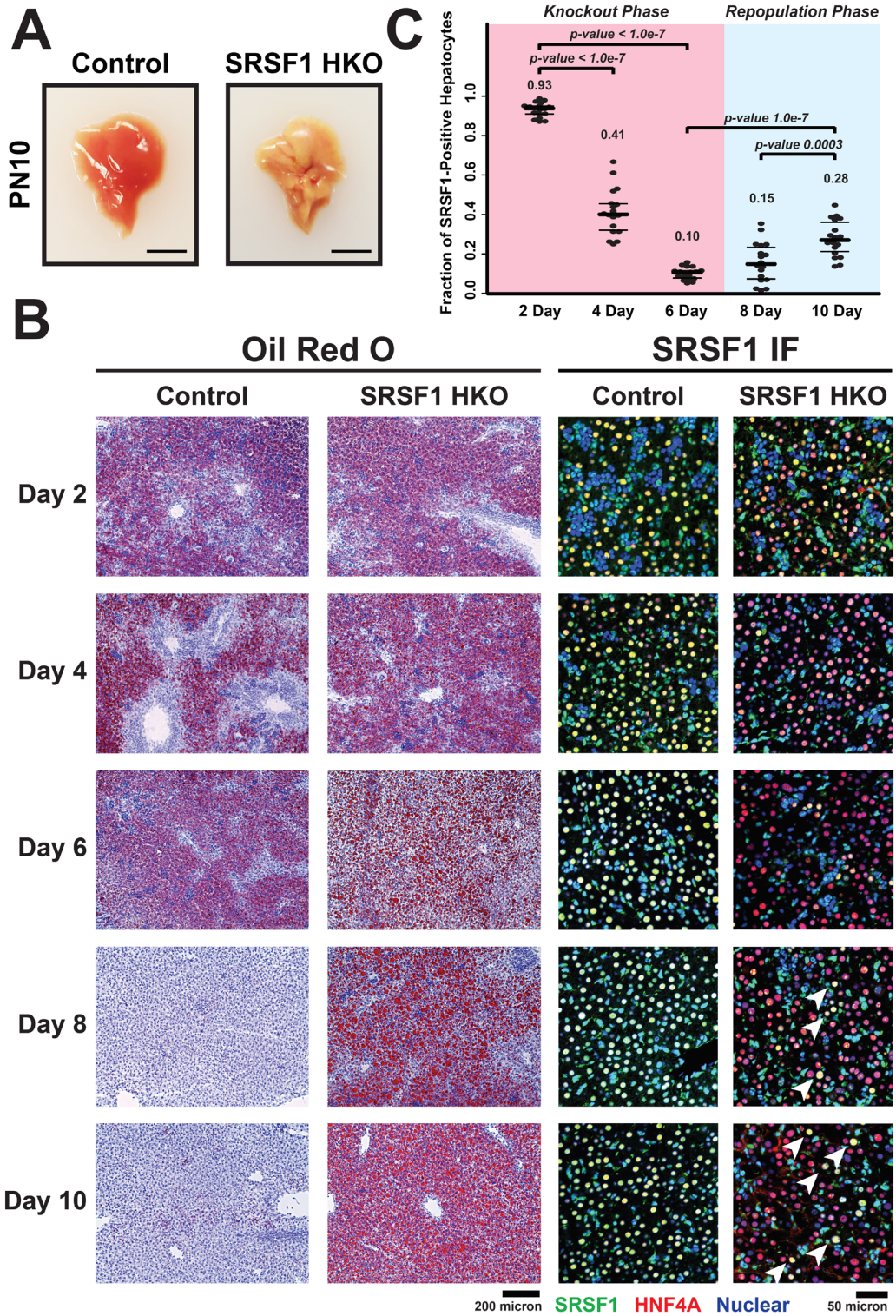

Fig. 1. Knockout of SRSF1 in hepatocytes triggers a regenerative response. (A) Representative gross images of livers harvested from Control (*AlbCre*$^{+/-}$) and SRSF1 HKO (*SRSF1*$^{flox/flox}$; *AlbCre*$^{+/-}$) mice 10 days after birth (n = 6 per group). Scale bar = 1 cm. **(B)** Representative histological (Oil Red O) and immunofluorescence (IF) images of liver sections from Control and SRSF1 HKO mice at indicated timepoints (n = 3 per group, 6 fields per replicate). IF images show co-staining with SRSF1 (green), HNF4α (red), and Nuclei (blue). White arrows indicate repopulation of tissue with SRSF1-expressing hepatocytes. **(C)** Quantification of the fraction of SRSF1-expressing hepatocytes per field from IF images at each timepoint. Values are displayed as mean ± SD.

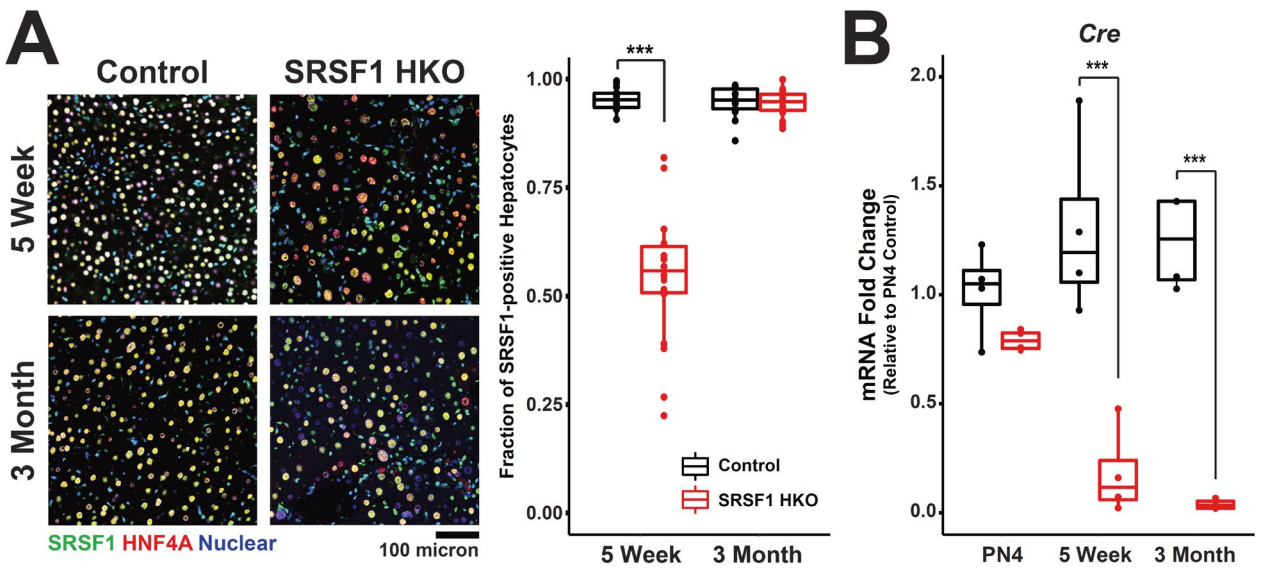

Fig. 2. Hepatocytes in SRSF1 HKO mice eventually circumvent knockout via AlbCre repression. (A) *Left:* Representative IF images of liver sections from Control and SRSF1 HKO mice at indicated timepoints (n = 3, 6 fields per replicate). IF images show co-staining with SRSF1 (green), HNF4α (red), and Nuclei (blue). *Right:* Quantification of the fraction of SRSF1-expressing hepatocytes per field from IF images at each timepoint. **(B)** Relative mRNA expression (qPCR) of AlbCre normalized to *36B4* expression in Control and SRSF1 HKO mice (n = 4 mice per group) at the indicated timepoints. Values are displayed as mean ± SD. PN4, post natal day 4.

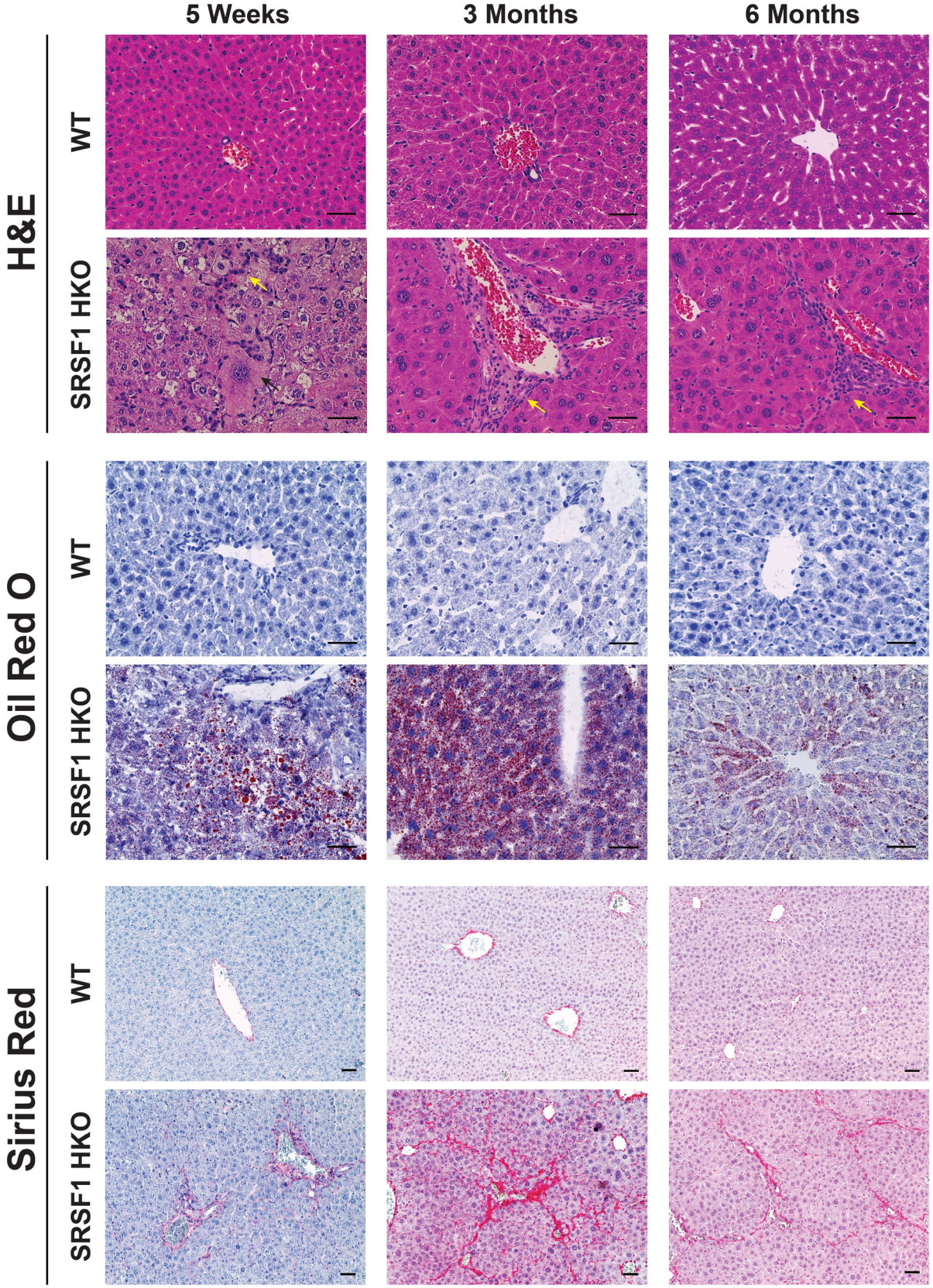

Fig. 3. Acute and reversible NASH-like pathology in adult SRSF1 HKO mice. Representative images of H&E, Oil Red O (red, neutral lipids), and Sirius Red (red, collagen) histological staining of liver tissue harvested from wildtype (WT) and SRSF1 HKO mice at the indicated ages (n = 6 per group). Yellow and black arrows in H&E staining indicates inflammatory infiltration and ballooning degeneration, respectively. Scale bar = 100 micron.

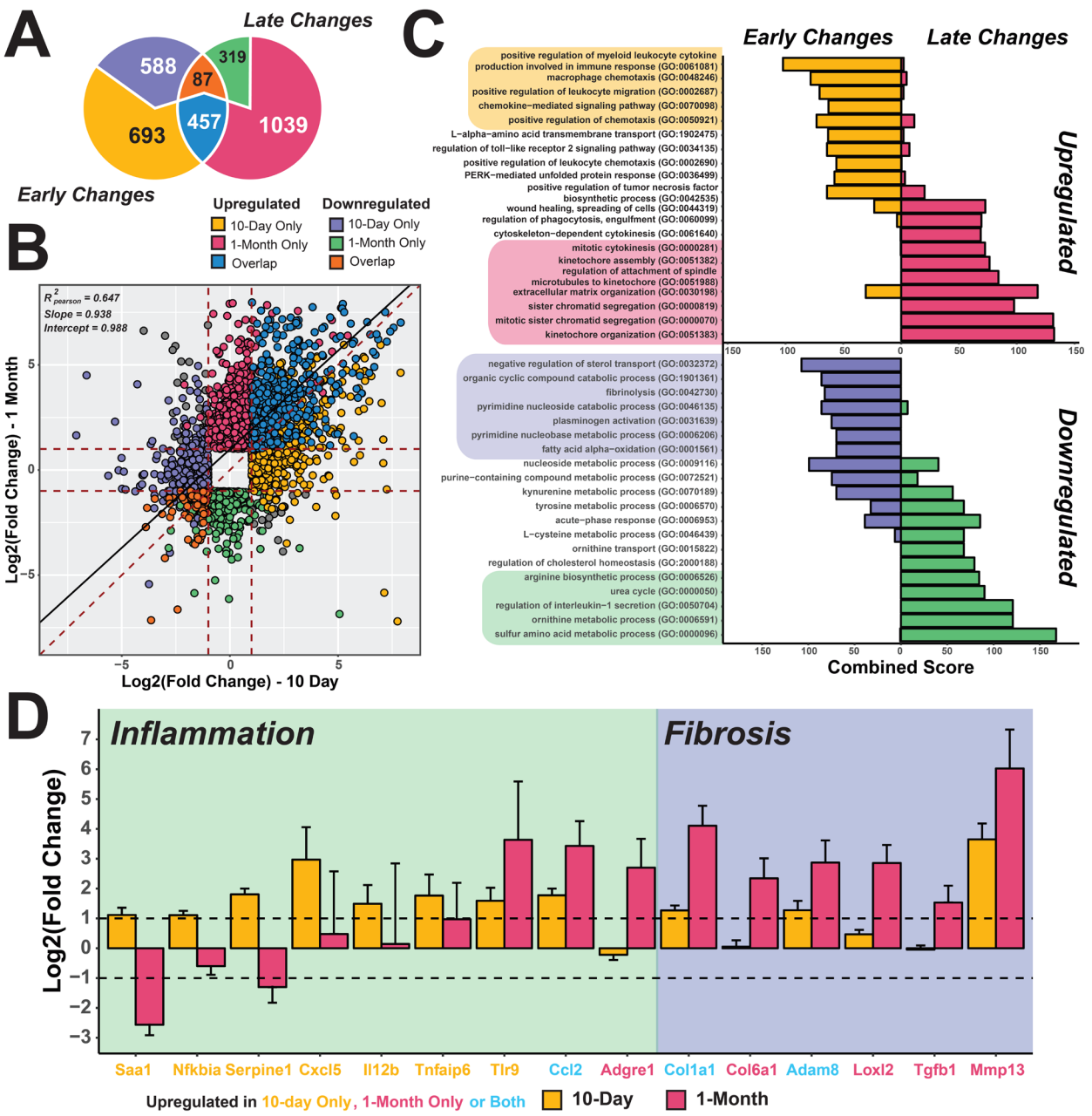

Fig. 4. Gene expression signatures in SRSF1 HKO hepatocytes transition from an early inflammatory to a late fibrotic phase. (A) Overlap of differentially expressed genes from RNA-seq (FDR < 0.05, Wald test as described DESeq2; $|\text{Log}_2(\text{Fold Change})| \geq 1$) in 10-day (early) and 1-month (late) old SRSF1 HKO hepatocytes (n = 2 samples/condition). **(B)** Scatter plot showing the distribution of mRNA abundance fold changes in SRSF1 HKO with respect to controls at both early and late timepoints. **(C)** Gene ontology (GO) terms of upregulated and downregulated genes in SRSF1 HKO hepatocytes at 10-day and 1-month or early and late, respectively. **(D)** Bar plot of fold change values determined from RNA-seq analysis for genes involved in inflammation and fibrosis at both early (yellow bars) and late (red bars) timepoints. Color of gene labels signify significant upregulation in mRNA abundance at 10-day only (yellow), 1-month only (red), or both (blue).

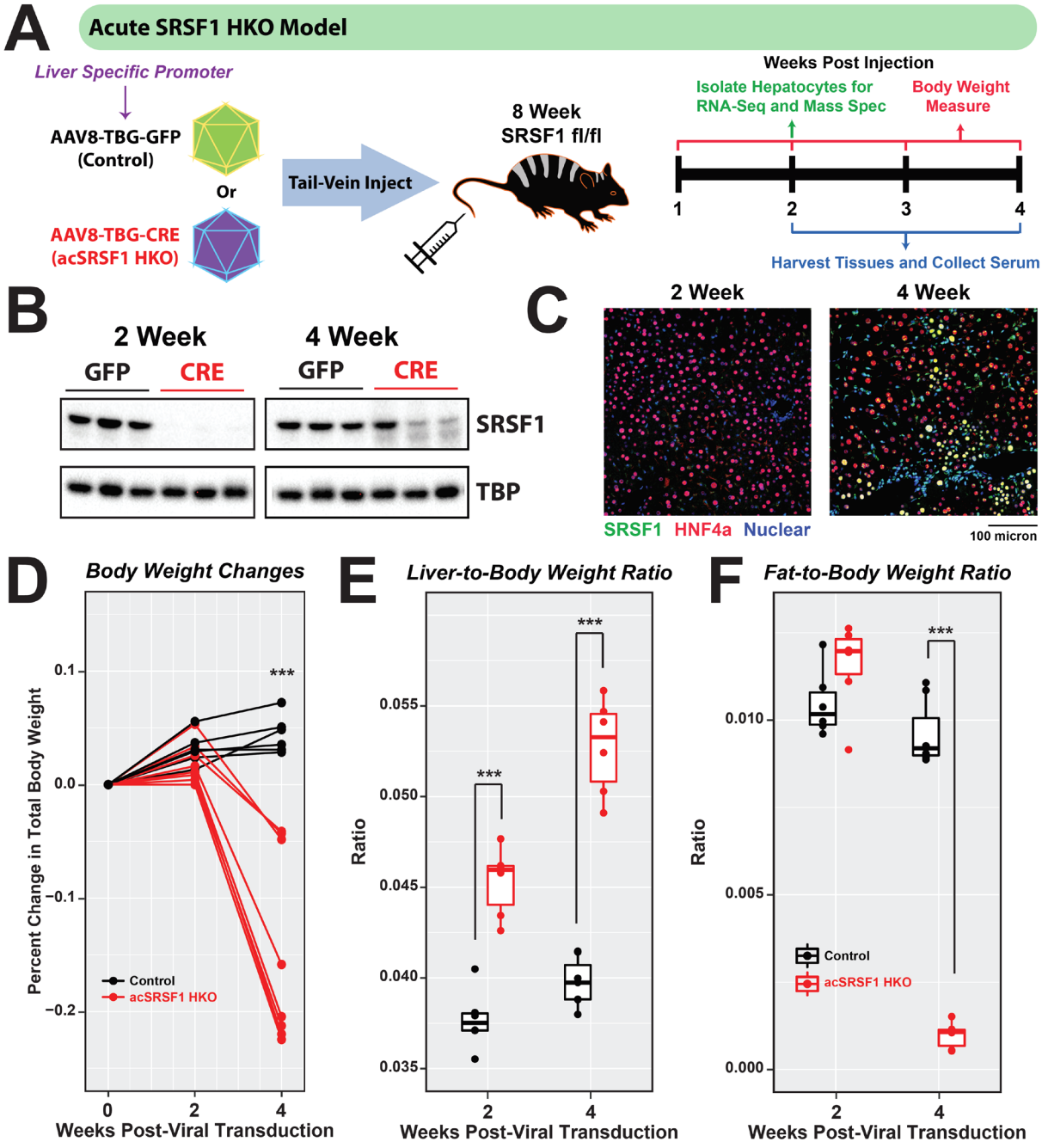

Fig. 5. Generation and characterization of mice with acute hepatocyte-specific knockout of SRSF1. (A) Schematic description of acute hepatocyte-specific SRSF1 knockout (acSRSF1 HKO) mice model and experimental design. Transgene expression is driven by the liver-specific thyroxine binding globulin (TBG) promoter. **(B)** Western blot showing hepatic SRSF1 protein levels in acSRSF1 HKO (CRE) relative to controls (GFP) at the indicated timepoints post viral transduction. TBP served as a loading control. **(C)** Representative IF images of liver sections from acSRSF1 HKO mice at indicated timepoints (n = 5, 6 fields per replicate). IF images show co-staining with SRSF1 (green), HNF4α (red), and Nuclei (blue). Yellow nuclei indicate SRSF1-positive hepatocytes. **(D)** Plot of percent change in total body weight at indicated timepoints. Weight before viral transduction is considered baseline. Box plots of **(E)** liver-to-body weight and **(F)** gonadal fat-to-body weight ratio in control and acSRSF1 HKO. Two-tailed unpaired *t* test with Bonferroni correction was used to determine significance between 2 groups. **P* < 0.05, ***P* < 0.01, ****P* < 0.001.

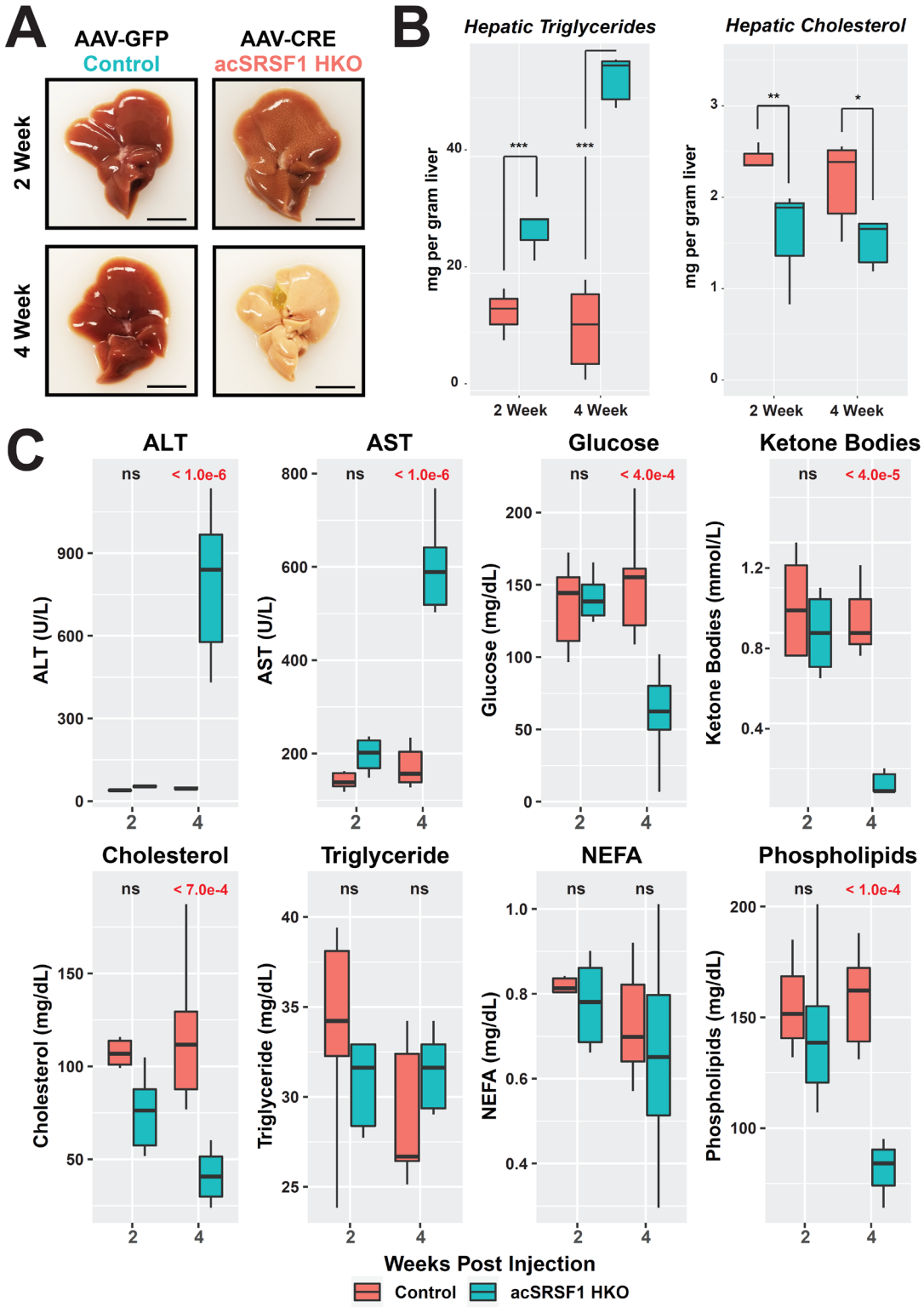

Fig. 6. Acute SRSF1 HKO mice develop hepatic steatosis and liver failure. (A) Representative gross images of whole livers harvested form control and acSRSF1 HKO mice at the indicated timepoints. Scale bar = 1 cm. **(B)** Box plot of measured hepatic triglyceride and cholesterol levels in control and acSRSF1 HKO mice (n = 6 – 8 per group). **(C)** Profiling of the indicated metabolic parameter in serum collected from control and acSRSF1 HKO after 6 hours of fasting at the 2- and 4-week timepoints. Two-way ANOVA statistical test was used to determine significance between 2 groups at 2 timepoints. P-values are listed above each comparison. *$P < 0.05$, **$P < 0.01$, ***$P < 0.001$.

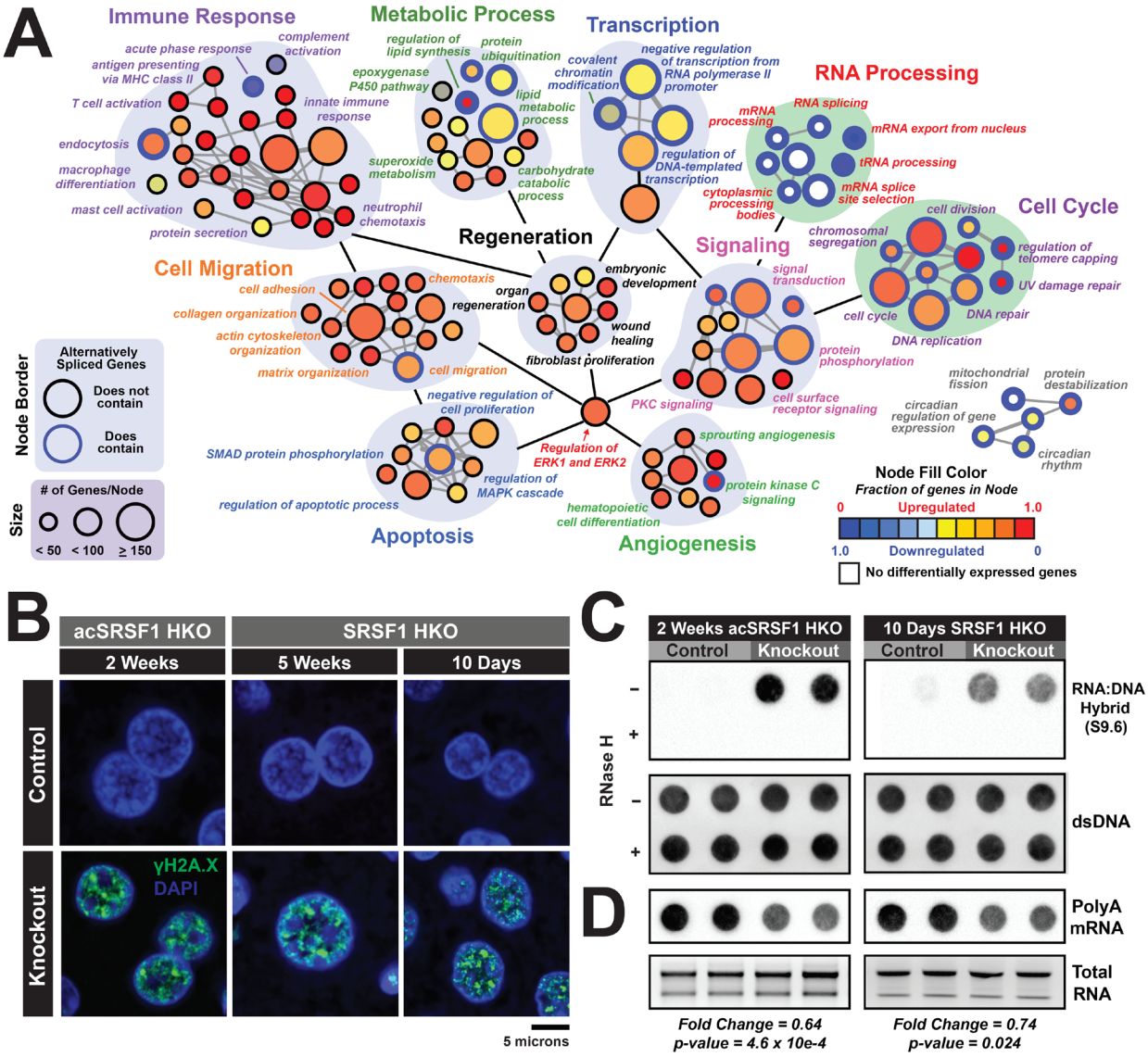

Fig. 7. Loss of SRSF1 results in DNA damage mediated by R-loop accumulation. (A) Gene ontology network map showing biological processes enriched for genes with differential expression or exon splicing in acSRSF1 HKO hepatocytes. Each node corresponds to an enriched GO term with the size and color representing the number of genes within the node and the direction of differential expression, respectively. Nodes with blue outline signify nodes that contain genes with differential splicing events in acSRSF1 HKO. **(B)** Representative IF images of liver sections from acSRSF1 HKO and SRSF1 HKO (n = 4-5 per group) at the indicated timepoints probed for γH2A.x (green), a DNA damage marker, with nuclear counterstaining using DAPI (blue). **(C)** Representative dot blots showing detection of R-loops in purified DNA from control and SRSF1 knockout samples (n = 4 per group) using the S9.6 antibody that recognizes RNA:DNA hybrids. As a negative control, half of each DNA preparation was treated with RNAse H. Corresponding dot blot for dsDNA was performed to confirm equal loading. **(D)** Dot blot analysis of polyA$^+$ mRNA on purified total RNA using a polydT probe to assess relative steady state levels of transcribed mRNA. Total RNA gel electrophoresis is shown for confirmation of equal loading. Values signify mean relative fold change between knockout and control.

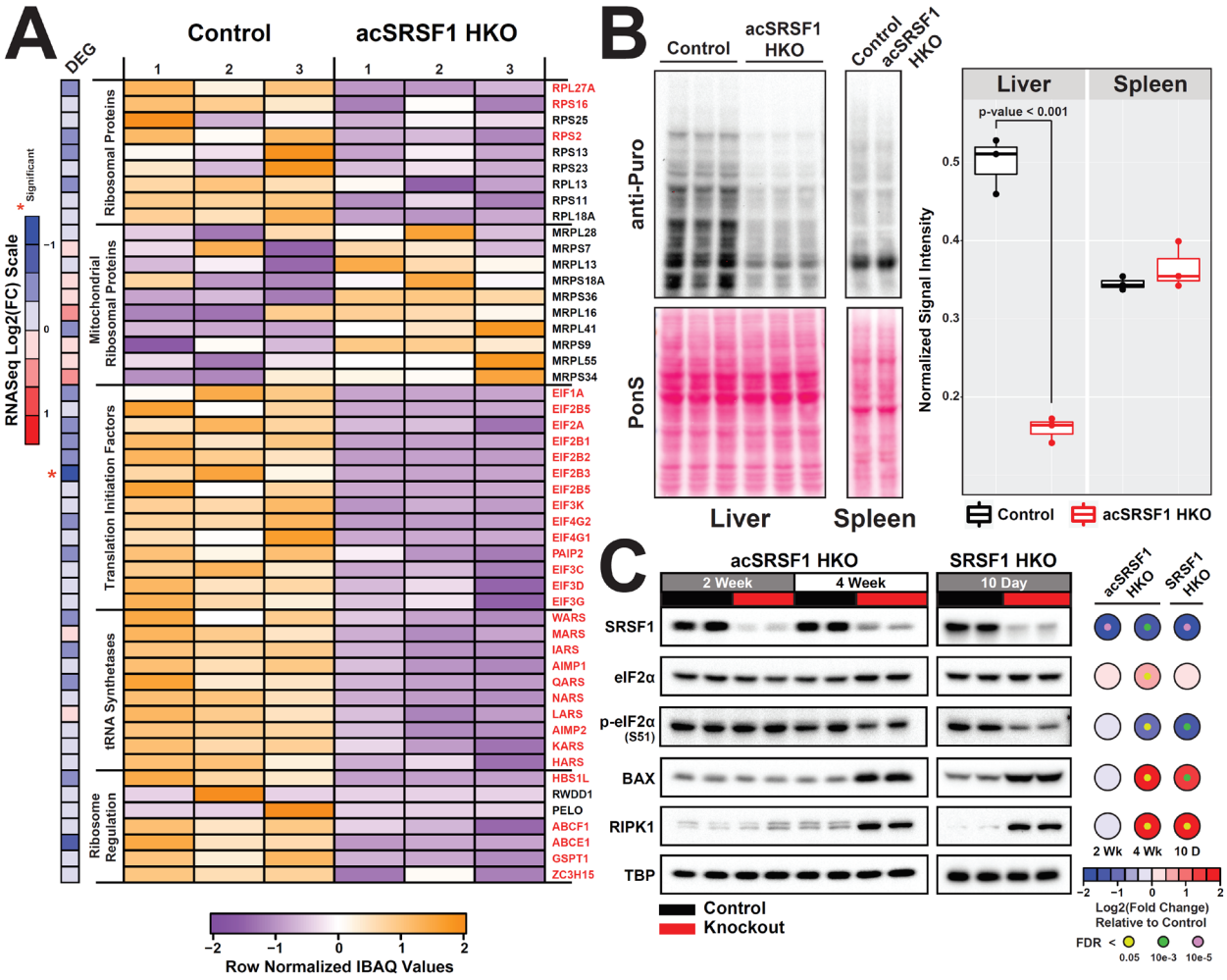

Fig. 8. Acute SRSF1 HKO hepatocytes display striking defects in global translation. (A) Heatmap depicting relative protein abundances based on calculated IBAQ values (row normalized) of various factors involved in translation from mass spectrometry of control and acSRSF1 HKO hepatocytes (n = 3, per group). Factor labeled in red indicate significant difference in abundance ($Log_2|Fold\ Change| \geq 1$, FDR < 0.05) between control and knockouts. Heatmap strip on the left shows relative fold change of mRNA abundance of the associated factor. **(B)** Measurement of de novo protein synthesis using a puromycin incorporation assay on hepatocytes isolated from control and acSRSF1 HKO at the 2-week timepoint. Spleens were harvested as well and are used as a control tissue. Relative nascent protein synthesis was quantified as the total signal ratio of puromycin labeled peptides (anti-puromycin) to total protein (Ponceau S). **(C)** Representative western blots of indicated factors on control and SRSF1 knockout hepatocytes isolated from 2- and 4-week acSRSF1 HKO and 10-day SRSF1 HKO mice models (n = 4, per group). Heatmap displays quantification of average fold change of protein abundance in SRSF1 HKO relative to controls. Colors of the large and small nodes signify average fold change and false-discovery rate, respectively.

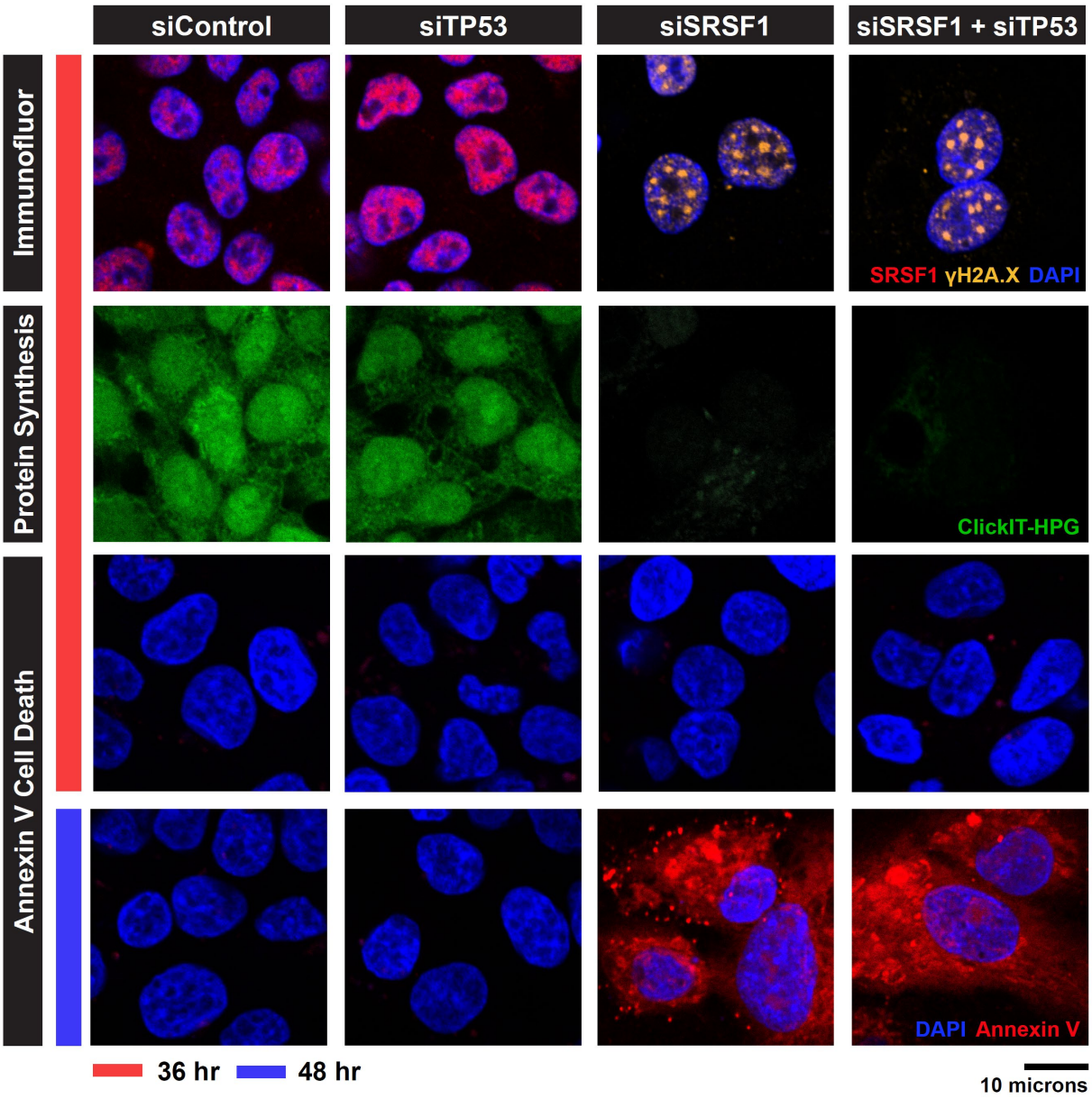

Fig. 9. Acute knockdown of SRSF1 in HepG2 recapitulates SRSF1 HKO pathology. HepG2 cells were cultured and treated with the indicated siRNA for 36 and 48 hours before performing the specified assays. First Row: Immunofluorescent staining for SRSF1 (red), γH2A.X (yellow), and nuclear (blue) after 36 hours of knockdown with the specified siRNA. Second Row: Qualitative assessment of nascent protein synthesis (green) of the same field shown in the first row using a fluorescent based ClickIT-HPG incorporation assay. Third and Fourth Rows: Annexin V staining (red) for cell death of HepG2 cells at 36 and 48 hours post knockdown by the specified siRNAs. All images shown are representative of n = 3 replicates x 5 fields per group.

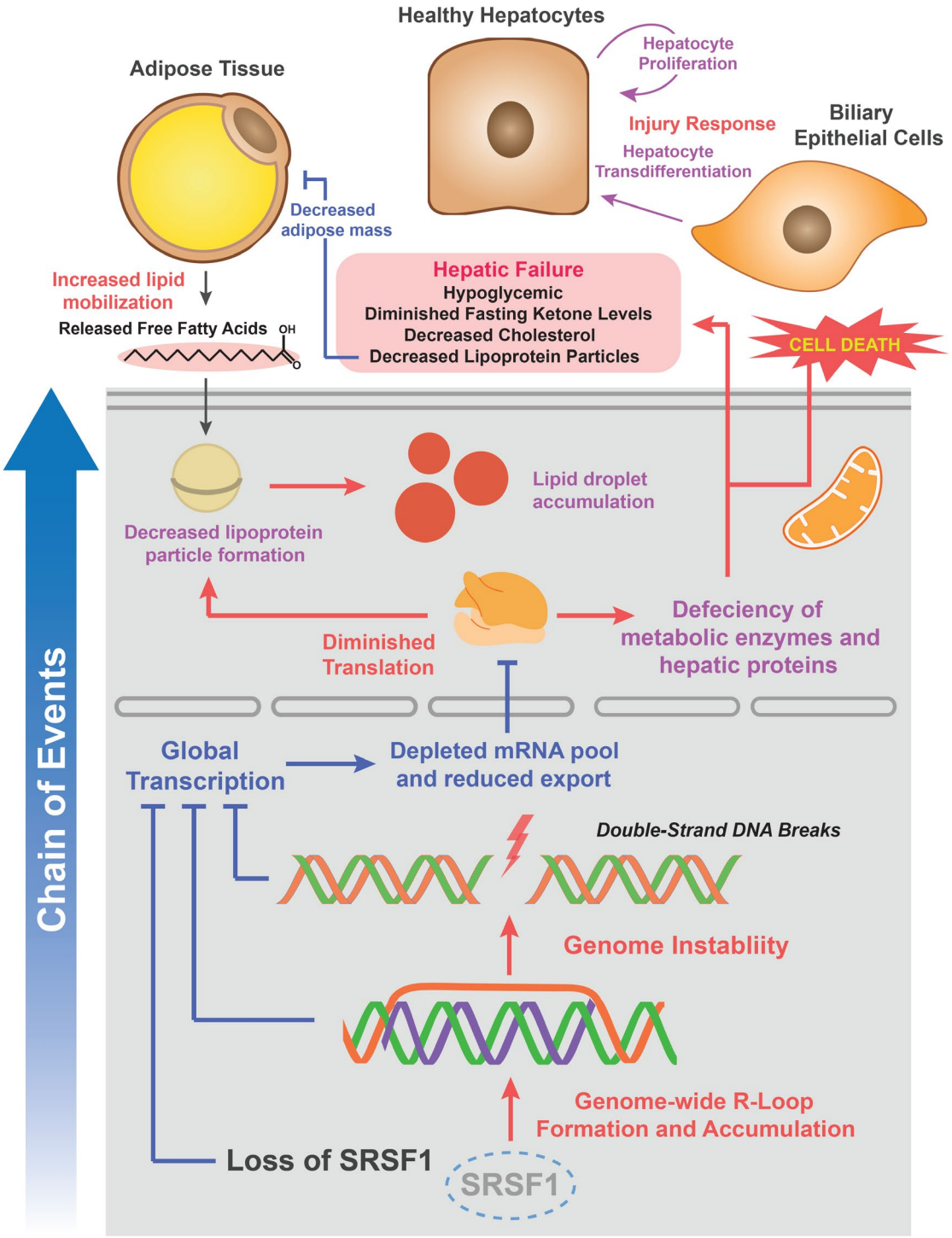

Fig. 10. Proposed mechanism of cell death in SRSF1-deficient hepatocytes. Loss of SRSF1 initially leads to an overwhelming accumulation of R-loops within the actively transcribed DNA of hepatocytes. This results in widespread DNA damage as unresolved R-loops are prone to double stranded breaks. The combined effects of SRSF1 activity loss, R-loop accumulation, and DNA damage response causes a halt in global transcription. With decreased mRNA synthesis and export, there is diminished translation and protein production which leads to subsequent cell death and hepatic failure.